

ETH ZÜRICH

BACHELOR THESIS - SPRING SEMESTER 2020

CHAIR OF EARTH OBSERVATION AND REMOTE SENSING

---

# Property extraction of retrogressive thaw slumps in the Canadian high Arctic using TanDEM-X and ArcticDEM data

---

*Author:*

Giorgio LAGHI

*Supervised by:*

Philipp BERNHARD

Prof. Dr. Irena HAJNSEK

29. May 2020

glaghi@student.ethz.ch

## **Acknowledgements**

A special thanks goes to my supervisor Philipp Bernhard, who has guided me through all my work. His valuable advice and experience have helped me to complete my thesis, but above all, they will also be useful to me in the future. My gratitude also goes to Prof. Dr. Irena Hajnsek and the whole Earth observation department for allowing me to write my thesis in this interesting field.

## **Abstract**

Large areas of the Canadian high Arctic are undergoing rapid surface changes as increases in summer temperatures lead to permafrost thaw. Retrogressive thaw slumps constitute one of the most dramatic and rapid manifestations of permafrost degradation. In the years following the initialization, these slumps continue to expand during the summer months, enabling them to be monitored by comparing digital elevation models over time. We present an analysis of the use of digital elevation models generated from remote sensing observation for the extraction of slumps properties like headwall height, retreat rate and volumetric change. 14 slumps located in the Eureka Sound Lowlands have been considered using data acquired by TanDEM-X and ArcticDEM between 2009 and 2017. These observations have provided a mean retreat of 10.8 m/y and an average headwall height of 6.9 m. A comparison of the retreat rates with a previous study conducted in the same area showed good consistency of the results. A major limitation have been identified in the lack of regular observations covering the whole area. Repeated observations on a pan-Arctic scale are essential to monitor the changes occurring in permafrost regions.

# Contents

<b>1</b>	<b>Introduction</b>	<b>1</b>
<b>2</b>	<b>Study Site &amp; Data</b>	<b>2</b>
2.1	Study Area . . . . .	2
2.2	Digital Elevation Models . . . . .	3
<b>3</b>	<b>Methods</b>	<b>4</b>
3.1	Data Processing . . . . .	4
3.2	Properties extraction . . . . .	5
<b>4</b>	<b>Data availability</b>	<b>6</b>
<b>5</b>	<b>Results</b>	<b>7</b>
5.1	Accuracy Statistics . . . . .	7
5.2	DEM differencing . . . . .	8
5.3	Properties extraction . . . . .	9
5.3.1	Headwall ablation . . . . .	10
5.3.2	RTS growth dynamics . . . . .	10
5.3.3	Retreat rates . . . . .	12
5.4	Validation to Jones <i>et al</i> 2019 . . . . .	13
<b>6</b>	<b>Discussion</b>	<b>14</b>
6.1	RTS activity . . . . .	14
6.2	Properties extraction . . . . .	14
6.3	Data accuracy . . . . .	15
<b>7</b>	<b>Conclusion</b>	<b>16</b>
<b>Appendices</b>		<b>i</b>
<b>A</b>	<b>RTS locations</b>	<b>i</b>
<b>B</b>	<b>Data Specifications</b>	<b>ii</b>
<b>C</b>	<b>Data availability</b>	<b>iii</b>
<b>D</b>	<b>Accuracy statistics</b>	<b>iv</b>
<b>E</b>	<b>Additional Locations</b>	<b>vi</b>

## 1 Introduction

Northern regions are characterized by a scarce vegetation, causing the soil to become extremely sensible to climate conditions. The presence of permafrost, which is defined as ground that remains at or below 0° C for two or more years, may lead to the formations of particular landforms [1]. Permafrost terrain consist in a surface active layer, extended in depth from a few centimetres to several metres, as shown in figure 1b. The active layer is sensible to seasonal climate changes, thawing in part during the summer and then refreezing in winter, acting as insulation for the perennial frozen ground [1]. Higher temperatures in the summer months can trigger the collapse of ice rich ground, leading to the formation of retrogressive thaw slumps (RTS). Initialization exposes further ground ice to summer ablation, mainly along the headwalls, which may lead to a subsequent enlargement of the slump [2]. Stabilization may occur in case the headwall reaches ice-poor terrain, or the accumulation of material isolates the ice-rich permafrost [3]. A warmer northern climate during recent decades has led to an increased RTS activity [4]. Particular relevance has been given to permafrost thaw because of the feedback on climate change, which still remains uncertain [5]. The mobilization of organic carbon stored in the permafrost region, which could then be mineralized by microbes and lead to emission of CO<sub>2</sub> and CH<sub>4</sub> on a time scale of years to decade, might even accelerate global warming [6]. Furthermore, RTS activity significantly increases sediments and solutes concentrations downstream, critically impacting the aquatic ecosystems [7] [8].

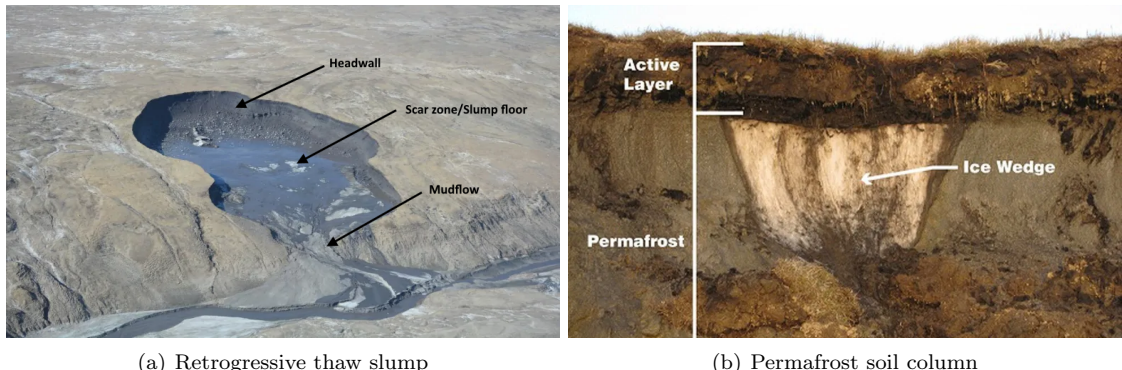


**Figure 1:** Areas in the high Arctic are characterised by scarce vegetation and a relatively thin active layer. Credits: Melissa Ward Jones & Benjamin Jones, USGS.

Permafrost thaw mostly occurs in remote and hardly accessible areas with severe climate conditions, making remote sensing highly important for investigating RTS activity. Furthermore RTS activity induce significant topographic changes, making them well detectable by differencing digital elevation models over time. The development of stereo satellite imagery in recent years has enabled the generation of 3D terrain models with a very accurate elevation. The rapid development of satellite systems, with an increase in sensor resolution and time and spatial coverage, has additionally increased their appeal for monitoring RTS using remote sensing techniques. In this report, an attempt to extract slump properties like the headwall height, retreat rate as well as volumetric change using only remote sensing observations will be made. Additionally, the accuracy and feasibility of the results obtained will be evaluated.

## 2 Study Site & Data

### 2.1 Study Area

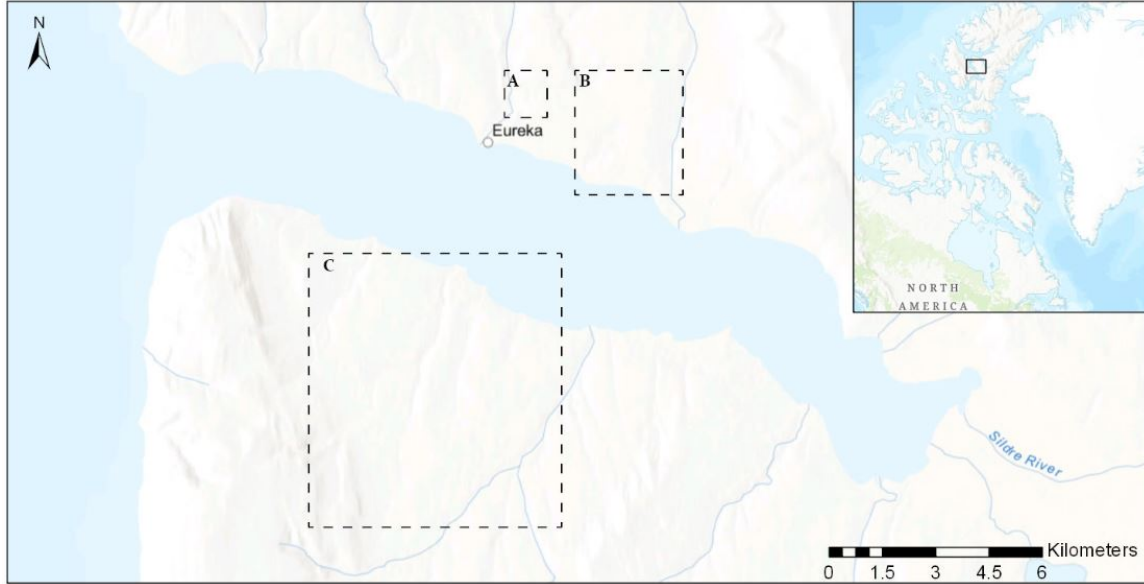


**Figure 2:** Map showing the Slidre Fjord in the Eureka Sound Lowlands, where the areas of the location of the RTS considered are denoted by the subsets A, B, C. The weather station is placed in the Eureka research camp.

Eureka Sound is a polar desert area situated on Ellesmere Island, one of the most northerly island in the Canadian high Arctic. A small research base is located on the north side of Slidre Fjord and is currently the third northernmost permanent base in the world. Eureka was established in 1947 and his weather station is recording daily meteorological measurements since then.

Mean daily temperatures were used from the Eureka meteorological station to compute the Thawing degree days (TDD) between the observations dates [9]. TDD were defined as the cumulative value of all mean daily air temperatures above  $0^{\circ}$  C between the observation dates. The long-term average thawing degree-days recorded from the Eureka station is 359 [10]. The climate is characterized by low rainfall, and the thaw season, defined as the period in which temperatures remain above  $0^{\circ}$  C, varies between 3 and 6 weeks, mainly in July and August [10]. Mean annual, January and July air temperatures since 1947 are  $-19.7^{\circ}$  C,  $-36.1^{\circ}$  C and  $+5.4^{\circ}$  C respectively [11]. The measurements of recent years show a gradual increase in temperatures. The monthly average for July over the last 10 years is  $7.7^{\circ}$  C, in particular due to record summer warmth in 2011 and 2012, which promoted a rapid RTS initialization [10]. In 2011 and 2012 the average air temperature in July was  $9.8^{\circ}$  C and  $8.7^{\circ}$  C respectively, well above the mean of the historical records.

Permafrost in the Eureka Sound is continuous, relatively cold and deep, with an estimated thickness of over 500 m. The active layer is relatively thin, measuring approximately 60 cm [10]. The number of RTS located in the region is estimated to be around 200, half of which have been formed since 2011 [11]. The studied area selected in figure 2 has an extension of around  $53 \text{ km}^2$ . 20 slumps contained in the three subsets have been selected, and their exact location is indicated in

Appendix A. RTSs 1-12 are contained in subsets A and B and were already included in a previous study, thus will also be used as validation. The remaining 8 were mainly selected in the southern side of the Fjord in order to extend our research.

## 2.2 Digital Elevation Models

Digital elevation models (DEM) generated from TanDEM-X radar observations as well as from ArcticDEM optical stereographic imagery were used to extract slump properties between 2009 and 2017. A complete list of the DEMs used is presented in section B of the appendix.

TanDEM-X is a formation of two twin satellites, and DEMs are generated using single pass synthetic aperture radar (SAR) interferometry [12]. In the single-pass bistatic mode, an antenna emits a radar signal which is then observed at the same time by both satellites separated by a variable baseline [8]. Single pass SAR prevents inaccuracies due to atmospheric disturbance and spatial decorrelation, which are instead common problems in a repeat-pass mode [13]. The phase difference between the two radar signals acquired from slightly different spatial positions is then scaled to height variations, in order to generate digital elevation models. Using active remote sensing, TanDEM-X is operating in the X-band at a wavelength of 3.1 cm. The spatial resolution is around 12m x 12m with a vertical accuracy of 2 m for a relatively flat terrain. For slopes of more than 11 degrees the vertical accuracy may increase to 4 m [13].

ArcticDEM's data are generated using high-resolution optical images acquired by Digitalglobe's polar-orbiting satellites. Being a passive system it depends on solar radiation and cloud coverage. DEM's are created using in-track stereo imagery collected by Worldview 1-3 and GeoEye-1 satellite sensors [14]. Stereographic pairs are acquired from different angles about 45-90 seconds apart. A DEM extraction algorithm, Surface Extraction with TIN-based Search-space Minimization (SETSM), is then used to extract a 3D elevation model of the area [15]. Each pixel is matched to the corresponding one from the other image taken from a different angle, in order to determine the surface elevation. Surface outliers due to an incorrect matching are already substantially reduced as a further step of the SETSM [16]. Spatial resolution is 2m x 2m with a vertical accuracy of 4 meters.

### 3 Methods

Data were processed using the programming language *Python 2.7* with *GDAL 2.3.3* extension to manipulate geospatial raster data. An earlier version of Python has been used in order to import ArcMAP functionalities in a Python environment using *Arcpy* library. Manual operations have been implemented in *Arcmap 10.7*. Headwall retreat rates were computed using the *Digital Shoreline Analysis System 5.0* (DSAS) software ArcGIS extension tool [17]. To compute general accuracy statistics slope and aspects were manually determined in ArcMAP and then the raster images were imported in Python.

#### 3.1 Data Processing

ArcticDEM data were directly downloaded from the ArcticDEM project website.<sup>1</sup> To reduce the amount of data only the strips covering our area of interest were selected, intersecting the research area with the strip index file available on the ArcticDEM project website. Afterwards a translation vector was applied to the DEM files, to correct the offset to filtered IceSAT altimetry data. Translation vectors were already included among the downloaded data, although these translations were not yet applied to the DEM files. A coregistration between the DEMs itself was not implemented. At this point the selection process has been repeated for the single RTS clusters, but this time requiring a complete coverage of the area of interest.

TanDEM-X DEMSs were first reprojected to EPSG:3995 coordinates, the same of ArcticDEM data. Afterwards the data was resampled to the same resolution of 2m x 2m. These processes were needed in order to allow a direct comparison. Resampling to a higher resolution, however, did not improve the initial spatial resolution of 12m x 12m. Finally, all the DEMs were clipped to smaller polygons containing the single RTS clusters in order to speed up manual operations.

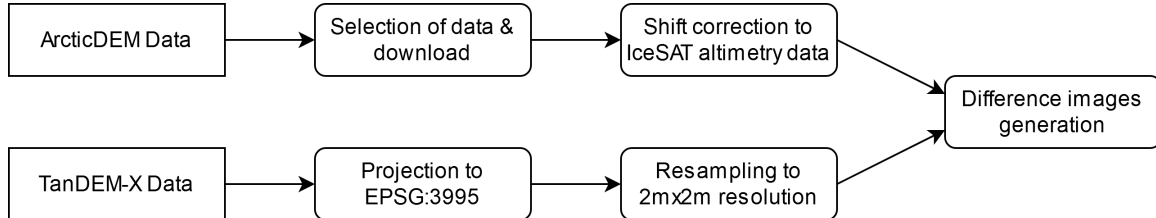


**Figure 3:** Overview of the process chain.

<sup>1</sup><https://www.pgc.umn.edu/data/arcticdem/>, [Accessed on May 2020].

### 3.2 Properties extraction

The operations required to extract RTS properties were mainly carried out in Arcmap. In principle, a DEM recorded in 2009 has been subtracted from those of the following years, thus serving as a reference. At this point it was possible to generate the difference images. In order to obtain statistics such as mean height and surface extent polygons covering the exact disturbed area were drawn manually for each observation. Mean height and surface extent were then used to estimate the volumetric change. Additionally, a transect line across the RTS was drawn to estimate the headwall height. Generally, the transect line was drawn in the middle of the RTS followig the headwall retreat direction, but random errors and sediments accumulation made in some cases a different positions necessary.

Retreats rates were computed with the DSAS extension tool, in which the headwall position was defined for every observation date, therefore representing a specific position in time. A baseline was also constructed as starting point for the transects subsequently generated by the DSAS application. Transect lines were generated with a transect spacing of 2 or 4 meters to measure retreat rates along each headwall. A smaller transect spacing was chosen in case of small RTSs, in order to obtain at least 10 measurements for each single slump. Transects were only generated along the initial extension of the headwall, hence the expansion along the flanks was not considered. Retreat rates are calculated in DSAS by using the distances between the reference baseline and each shoreline intersection along a transect, as shown in figure 4.

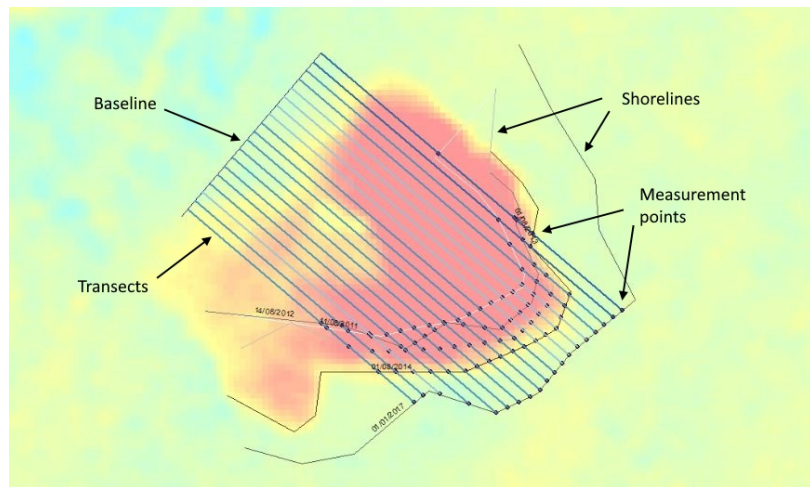


**Figure 4:** Retreat rates calculation with DSAS add-in for ArcMAP.

## 4 Data availability

Once all available observations were selected for each group of RTSs, it was possible to understand the time coverage of each specific location.

Three DEMs from TanDEM-X were available for the entire area, acquired in winter 2010-2011, 2011-2012 and 2016-2017 respectively. In winter there are optimal conditions for radar image acquisition, since the presence of a homogeneous snow pack with low water content ensures minimal influence on the propagation of radar waves.

The optical imagery of ArcticDEM have been differentiated between measurements recorded during the summer months, defined between mid-July and September, and the observations made in the rest of the year, as the presence of snow covered landscape can significantly affect optical observations. In the absence of observations acquired during the summer months, images acquired at the beginning of July were used and proved to be reliable. Images acquired during June, on the other hand, were not recorded, and therefore it was not possible to verify their accuracy. As discussed in more detail section 5.1, the images acquired at the beginning of spring contained a large error and were therefore not sufficiently accurate. Finally, a DEM generated at the beginning of October was also taken into account, but inaccuracies due to the presence of snow were observed. Unfortunately, under these conditions, annual coverage was not guaranteed. Annual measurements were possible only between 2009 and 2014. Furthermore, as can be seen in figure A4, the data availability may differ considerably depending on the precise area observed. Due to the longer time coverage for RTS 1-6, these were selected for validation with [11], which will be referred to as Jones *et al.* 2019. The remaining representations for additional RTSs were added as Appendix C.

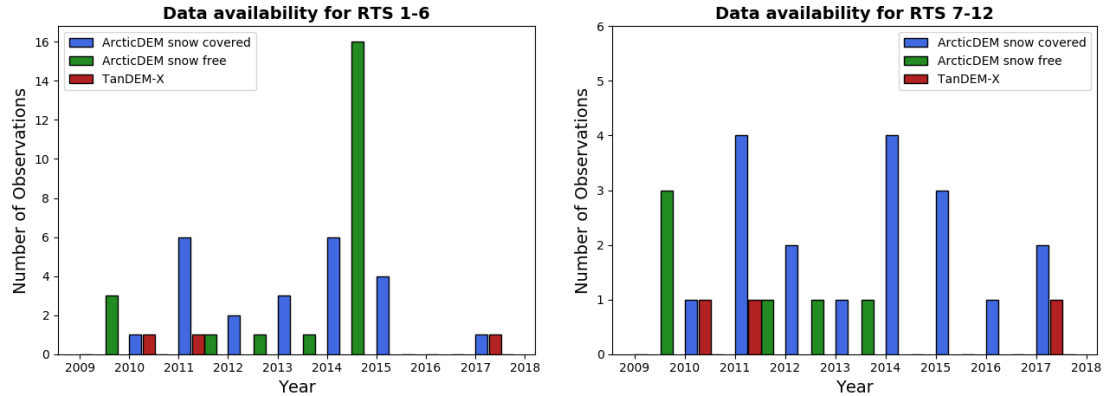


**Figure 5:** Data Availability of the researched area. The landscape was assumed snow free from the mid of July to September. Tandem-X observation where made in winter (2017 means winter 2016-2017).

## 5 Results

This section will first present the results of the accuracy statistics. Then the extracted properties of the individual slumps are included. Lastly a validation with a previous study will conclude the presented results.

### 5.1 Accuracy Statistics

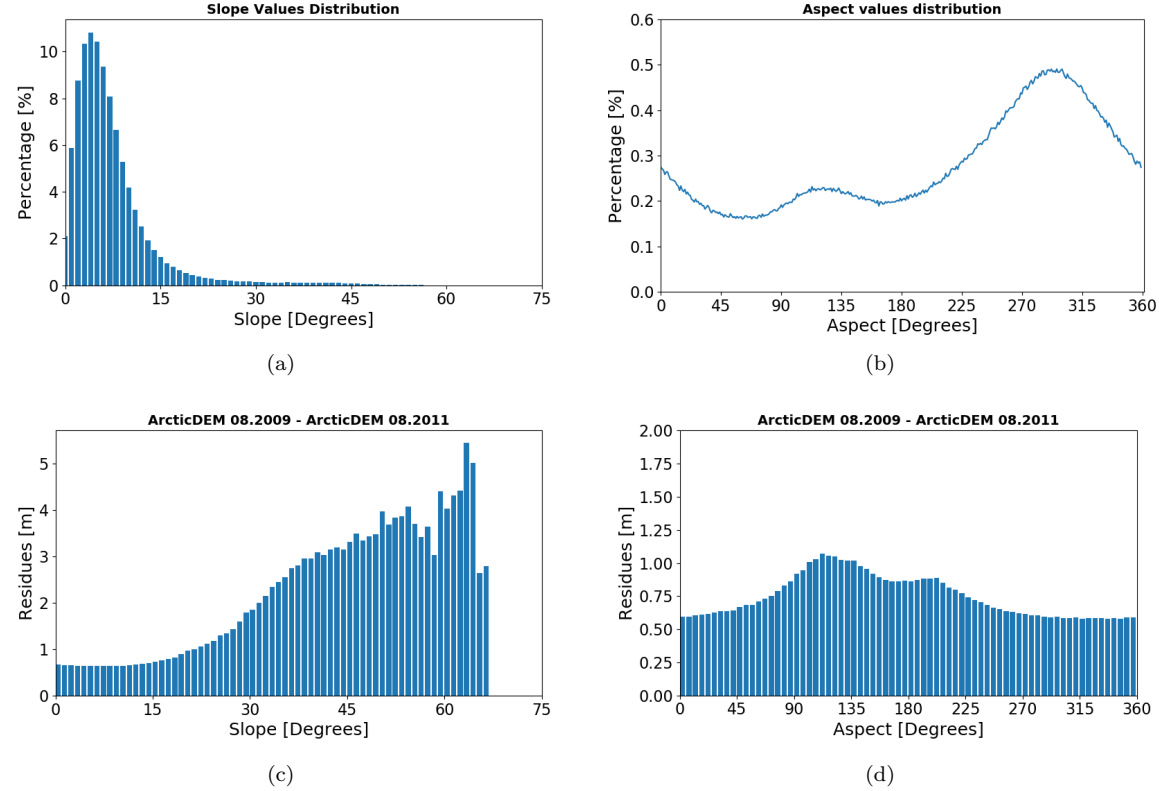


**Figure 6:** Accuracy statistics computed on test area 1. Figures a) & b) denote the occurrence of slope and aspect values in the area. Figures c) and d) instead represent the distribution of residues depending on the slope or aspect of a difference image generated with two ArcticDEMs acquired in summer. In the case of the aspect, 0 degrees indicates the north direction.

Figure 6 show general accuracy statistics computed on a test area near the slumps locations. Several difference images using different observations were generated, both TanDEM-X and ArcticDEM, in order to compute the residues distribution depending on the characteristics of the ground. The residues distribution shown in Subfigure 6 c) and d) correspond to the difference in height between two ArcticDEMs recorded in the summer months, and therefore assuming a snow-free landscape. Residues tend to increase for a steeper slope, while regarding the aspect, the values shows a maximum peak in the southeast direction. An uneven distribution of residues depending on surface orientation is mainly due to the orbit followed by the satellite. The remaining figures showing the distribution of residues for the other observations generated on test area 1 and 2 are included in the Appendix D. Generally, regarding the influence of the slope, starting from 15 degrees the residues tends to increase. The only difference images that do not show a clear dependency are those gener-

ated using optical imagery acquired in April, where the distribution of residues is more influenced by the thickness of the snowpack covering the area.

Mean residues and standard deviations are listed in Table 1. Due to the higher distribution of lower slope values the mean error tends to be less representative for steeper terrain, as can be seen by comparing the residues distribution with the mean residue in the case of ArcticDEM summer observations. This is not the case for aspect distribution, where the average mean residue seem to be a good approximation. Overall, the observations that performed best were those acquired by ArcticDEM in the summer months, followed by TanDEM-X observations and the combination of the two satellite systems using optical DEMs recorded in the summer months. The observations made by ArcticDEM in the spring months, on the other hand, proved to be unreliable, with an mean residual significantly higher than the others.

**Table 1:** Mean residuals  $\mu_{residue}$  and standard deviation  $\sigma$  computed on the test areas.

Observations	Area 1		Area 2	
	$\mu_{residue}$ [m]	$\sigma$ [m]	$\mu_{residue}$ [m]	$\sigma$ [m]
ArcticDEM 08.2009 - ArcticDEM 08.2011	0.71	0.83	0.61	0.49
ArcticDEM 08.2009 - TanDEM-X 2011	1.28	1.15	1.49	1.09
TanDEM-X 2011 - TanDEM-X 2017	1.19	1.30	1.25	1.08
ArcticDEM 04.2011 - ArcticDEM 08.2011	8.78	10.21	5.25	1.93

## 5.2 DEM differencing

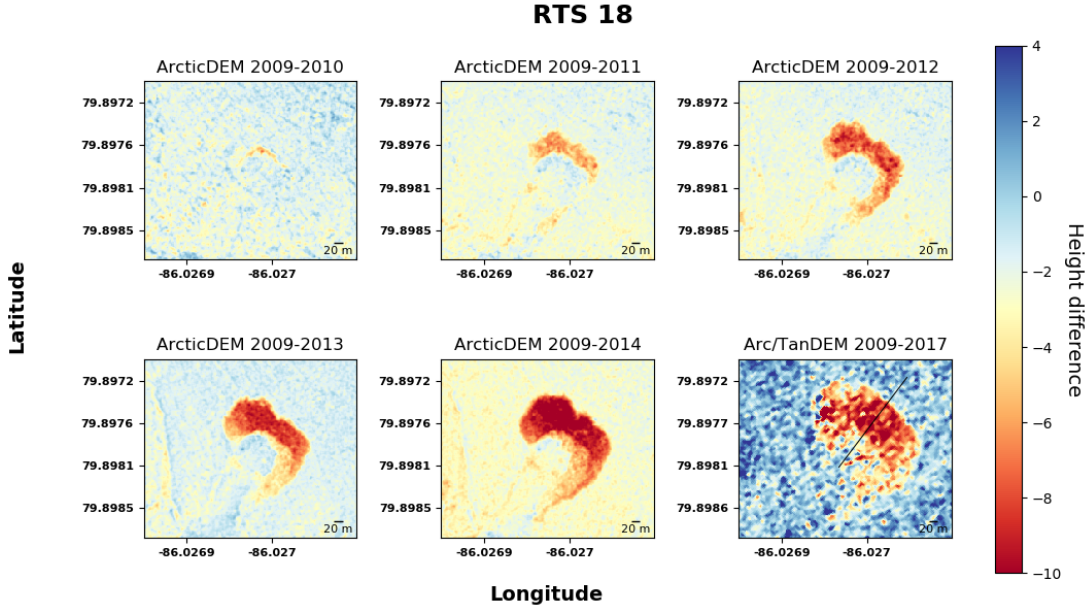


**Figure 7:** Evolution of RTS 18. The line drawn in the last image indicate the transect line used to generate the transect plot (see section 5.3.1)

20 RTS were selected in the study area, ranging from small in the order of a thousand square meters of disturbed area to larger in the order of tens of thousands of square meters. As a comparison, a soccer field has an area of about 7000 square meters. Difference images, volumetric change, headwall height and retreat rates were calculated for 14 of them. As an example RTS 18 will be used, the remaining ones are included in Appendix E.

Figure 7 shows the difference images between 2009 and 2017 of RTS 18. In this particular case, the initialisation seems to start already in 2010, but significantly increases from 2011. Headwall ablation continued in the following years without stabilize. Few sediments are observed in the lower part of the images. Some limitations are already visible if we consider the area around the RTS, which is not perfectly matching. The height shift of the DEMs range between 0 m and 3 m, and could affect substantially the statistics computed like for example the volumetric change.

### 5.3 Properties extraction

Table 2 summarises the various characteristics estimated for RTS 18. Area and volumetric change have been calculated cumulatively from 2009 until the second indicated date, while the retreat rate corresponds to the indicated period. Area, volume and headwall height of the slump increased throughout the entire study period, indicating a continuous RTS activity. Headwall retreat is correlated to the thawing degree days (TDD). Record summer warmth in 2011 and 2012 promoted rapid headwall retreat, which was later slowed down by the colder summer months of 2013 and 2014. The last headwall retreat is computed over a time span of 28 months, and therefore results in a higher value. TDDs for the individual years included in the last period correspond to 378° C, 565° C and 589.3° C for 2014, 2015 and 2016 respectively. The last two years have therefore recorded values significantly above the annual average, but without reaching the extreme values recorded in 2011 and 2012.

**Table 2:** Properties of RTS 18 between 2009-2017. Area and volume are cumulative.

Time period	Area [10 <sup>3</sup> m <sup>2</sup> ]	Vol. change [10 <sup>3</sup> m <sup>3</sup> ]	Headwall Height [m]	Headwall Retreat [m]	TDD [°C]
10.08.2009-01.07.2010	1.0	2.8	-	Init.	101.2
02.07.2010-11.08.2011	7.1	25.9	4.1	29.1	900.5
11.08.2011-14.08.2012	13.0	70.0	5.8	13.5	616.8
14.08.2012-01.08.2013	18.2	91.9	7.8	6.1	272.6
01.08.2013-01.08.2014	21.5	144.1	8.1	8.4	292.1
01.08.2014-01.01.2017	34.1	225.0	11.4	30.0	1292.8

Overall, the volumetric change ranged from 1 100 m<sup>3</sup>, as in case of RTS 3, to 225 000 m<sup>3</sup> in the case of RTS 18. Headwall heights varied between 1.9 and 12.5 meters. Retreat rates are analyzed separately in section 5.3.3. Most of the available observations were recorded at the beginning of August, thus in the middle of the thaw season, which makes difficult to clearly determine the initialization year. However, most of the observed slumps appear to have been initialized in 2011, with the exception of RTS 18, which seem to start already in 2010 and RTS 16 and 4 which may have been initialized in 2012.

### 5.3.1 Headwall ablation

A useful representation to detect headwall movement consists of a transect plot, as shown in figure 8. The transect line was generated following the headwall retreat direction, and can be clearly seen how the ablation occurs only along the headwall, retreating in one direction. The slump floor also lowered in this particular case, probably due to an elevated removal of sediments, which exposed further ground ice to solar radiation. The headwall height has been estimated by subtracting the value at the top of the headwall from one located at the end of the slump floor for each year. In this way it was possible to avoid the error due to the height shift of the various DEMs.

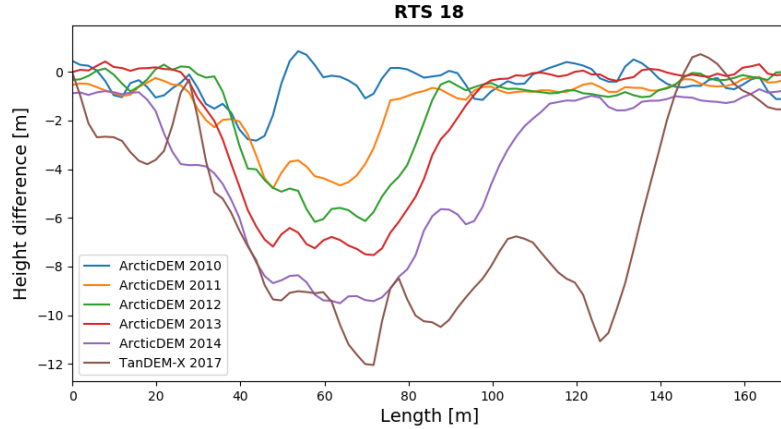


**Figure 8:** Height difference along the transect line

### 5.3.2 RTS growth dynamics

In order to be able to assess the evolution of the individual RTS considered, the volumetric change during the period of observation has been depicted, as shown in figure 9.

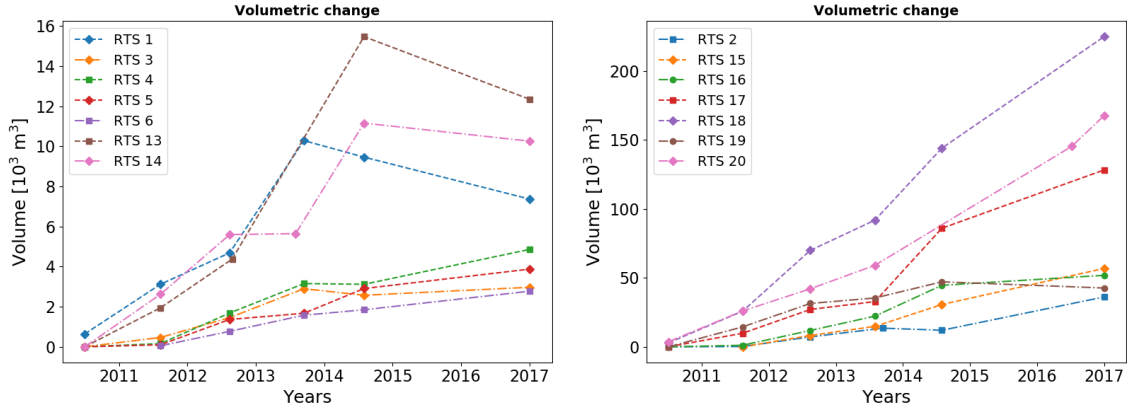


**Figure 9:** Volumetric change of the observed retrogressive thaw slumps between 2010 & 2017.

After the initialization of a slump, basically two outcomes can follow. The single RTS remains active, continuing to expose ground ice to melting and growing further, or it stabilises. Volumetric change is a good indicator to estimate the growth and activity of a single RTS, as it takes into account both surface extent and depth of the slumps, and therefore also allows to estimate the amount of mobilised material. However, its use requires not only a high accuracy of the individual DEMs, but also an accurate vertical and horizontal alignment between the DEMs time-series, since is detected by comparing digital elevation models over time. At least RTS 1, 13 and 14 shows an unreliable trend, likely affected by an inaccurate vertical alignment of the DEMs. Such a substantial increase despite the relatively cold summers of 2013 and 2014 is rather unlikely, neither is the following decrease between 2014 and 2017. An overestimation of the measurements in 2014 is also likely in several other cases, such as RTS 17 and 18, and is clearly visible when looking at the difference images. Due to a larger size, however, the values have not been so strongly influenced. Except for these measurements, no other evident anomalies are present, and the trajectories seem to be consistent with the other indicators. Most of the RTSs are still active between 2014 and 2017, except for RTS 3 and 19 that seem to stabilize. Unfortunately, the lack of measurements in 2015 and 2016 precludes a precise understanding of the RTS evolution in the latest years. In any case, it should also be considered that often the disturbed area does not increase proportionally to the headwall retreat, due to an enlargement of the headwall extent.

Another indicator to characterize thaw slumps consists of the headwall height, as shown in figure 10. Basically, two developments can be outlined. In case of RTS 1, 3-6 and 19, after a rapid formation the headwall recedes with a constant height. The remaining RTSs instead experienced a continuous headwall increase. A constant headwall, however, does not imply a stabilization of the RTS, but rather a growth on the horizontal plane, without a consequent lowering of the slump floor.

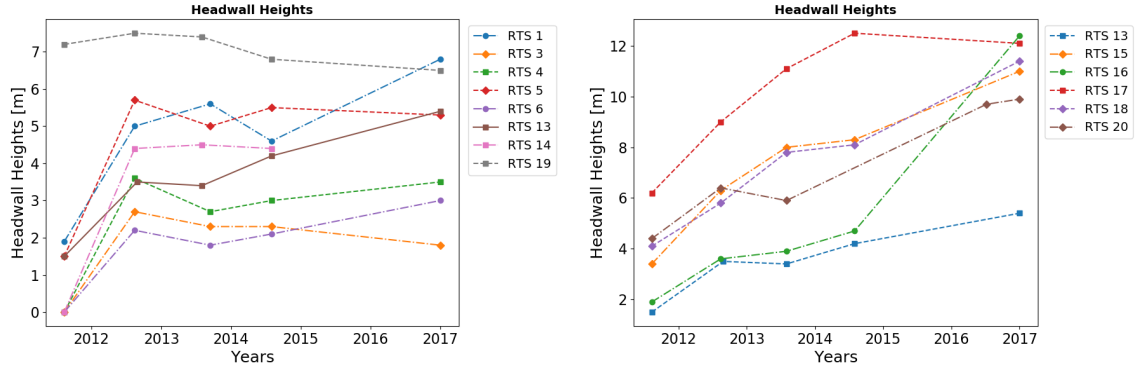


**Figure 10:** Headwall heights between 2011 and 2017

### 5.3.3 Retreat rates

The retreat rates determined for most of the RTS examined have been included in the table 3. The values in the case of RTS 18 are included in section 5.3, while in the case of RTS 20 due to significantly different dates they have not been included in this table and are present in Appendix E. An average annual retreat of 10.8 m/y for all RTSs was determined. Thaw slumps located south of the Fjord shows a higher activity, featuring higher retreat rates.

**Table 3:** Mean headwall retreat values for RTSs 1-6 & 13-19. The year shown correspond to the year of the second measurement were the headwalls were mapped and retreat rates were determined between the previous year and the year shown. TDDs may differ depending on the observation dates.

	RTS 1		RTS 2		RTS 3		RTS 4		RTS 5		RTS 6	
	Mean Retreat [m]	TDD	Mean Retreat [m]									
2011	Init.	900.5										
2012	13.3	616.8	15.7	616.8	24.2	616.8	11.3	616.8	8.2	616.8	19.4	616.8
2013	10.5	313.1	6.5	313.1	3.8	313.1	3.2	313.1	2.4	313.1	3.7	313.1
2014	2.8	247.1	4.8	247.1	7.3	247.1	5.2	247.1	6.1	247.1	7.0	247.1
2017	0.6	1292.8	28.3	1292.8	9.4	1292.8	11.7	1292.8	2.7	1292.8	9.2	1292.8
	RTS 13		RTS 14		RTS 15		RTS 16		RTS 17		RTS 19	
	Mean Retreat [m]	TDD	Mean Retreat [m]									
2011	Init.	900.5										
2012	8.5	681.6	22.8	616.8	10.6	616.8	13.3	616.8	7.1	616.8	33.4	616.8
2013	8.3	208.3	9.2	272.6	6.2	272.6	12.6	272.6	6.6	272.6	4.4	272.6
2014	5.8	279.2	10.1	292.1	11.7	292.1	5.9	292.1	8.3	292.1	11.0	292.1
2017	7.4	1292.8	30.6	1292.8	17.9	1292.8	17.8	1292.8	17.9	1292.8	29.0	1292.8

Higher retreat rates were generally identified in the year after initialization, at the corresponding time of warmer temperatures. In this period retreats rates of up to 30 m were measured. In 2013 and 2014 a sharp decrease has been observed, although values in the order of 10 meters have been measured. From 2014 onwards retreat rates are more differentiated, with some RTSs that seems continuing to gradually decrease and begin to stabilize, while other increases again. To note is that the last retreat rates between 2014 and 2017 were calculated along roughly two and a half thaw seasons.

#### 5.4 Validation to Jones *et al* 2019

The only study that provides results that allow to compare the values obtained is Jones *et al.* 2019, which determined the retreat rates of 6 RTSs also analyzed in this report. The retreat rates provided by Jones *et al.* 2019 have been determined using mainly differential GPS measurements, and are therefore particularly interesting to evaluate the accuracy of the values determined using only remote sensing observations. In table 4 the total retreat between 2010 and 2017 are listed. The mean difference over the entire observed period is around 5.0 m, with a standard deviation of 4.2 m. The computed values are all apparently overestimated, but remarkably approach the previous values in several cases.

**Table 4:** Total retreat in meters.

RTS	1	2	3	4	5	6
Jones	22.6	43.9	43	23.3	19.0	36.9
Computed	28.2	55.3	44.8	31.4	19.4	39.3

Since the observations given were not perfectly aligned, a direct comparison of the retreat rates recorded in individual years was not possible. Considering that the RTS activity is limited to a few weeks in the summer months and since measurements were performed exactly in this period, a shift of one month could already change the result significantly. Therefore, the results were represented with reference to the TDDs included in that period. In addition, in order to allow comparison in recent years the values have been recalculated in meters per year, as shown in figure 11. Since the data were adjusted to retreat per year, the values computed between 2014 and 2017 are the mean of the three retreat rates provided by Jones *et al.* 2019 in the same period. The average annual retreat for the 6 RTS is 7.8 m/y, while Jones *et al.* 2019 determined an annual mean retreat of 5.2 m/y.

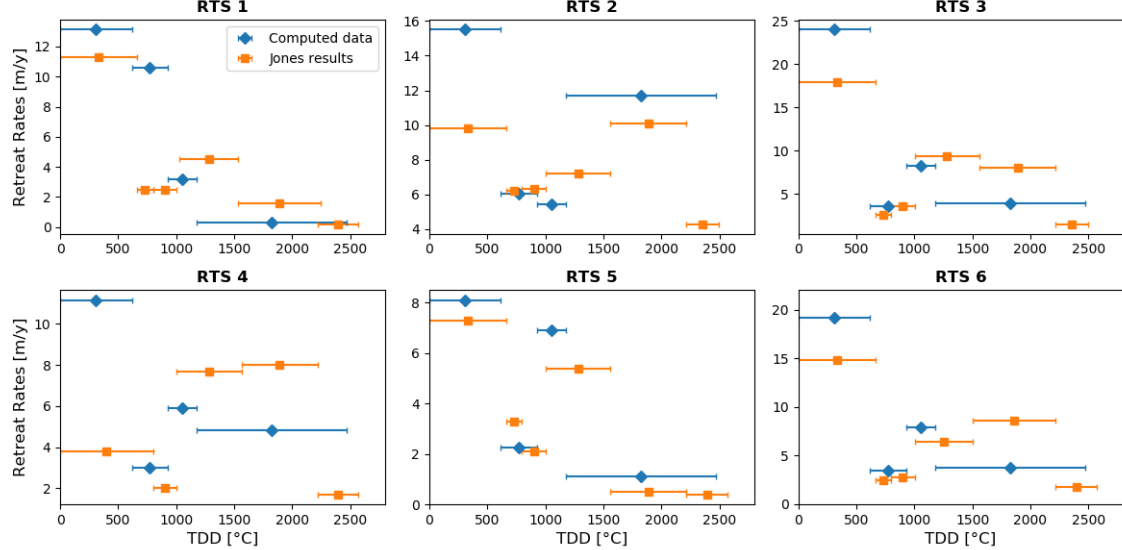


**Figure 11:** Comparison between the calculated data and the values obtained from Jones *et al.* 2019. The error bars indicate the TDDs recorded during the time span within the retreat rates was calculated. Jones *et al.* 2019 determined the retreat rate for every year between 2012 and 2017 and thus the interval length also indicates approximately the corresponding year.

## 6 Discussion

### 6.1 RTS activity

RTS activity in the high arctic is reduced to a few weeks in summer, and consequently the analysis of sub-seasonal dynamics is rather difficult. Several factors can affect the slumps activity, including climatic factors such as thawing degree days, annual rainfall and snowfall, as well as terrain factors such as ice-content of the soil, slope and surface orientation. Studies conducted in regions of the low arctic have shown a strong control of its activity by summer rainfall, which contributes to the removal of sediment while keeping the ice rich ground exposed [3] [18]. However due to the low precipitation in the Ellesmere area, RTS growth is limited, and seem to be more controlled by summer temperatures and terrain factors, such as slope, RTS morphology and aspect [11]. If climatic factors take place on a regional scale, affecting entire areas, the terrain factors, on the other hand, can lead to different developments of individual slumps under the same climatic conditions. Each individual slump must therefore also be considered individually.

According to Jones *et al.* 2019, a lack of precipitation would also limits headwall heights. The largest headwall height recorded in this report is 12.5 meters (RTS 17), with an average value for all RTS in 2017 of 6.9 m. Common headwall heights are around 5-10 m in the Eureka Sound area, while the highest headwall recorded is over 20 m [10].

The average annual retreat settles around 10 meters per year, which considering a higher activity of the RTSs south of the fjord are comparable to the results determined in previous studies. Jones *et al.* 2019 measured an average retreat for all 12 slumps of 6.2 m/y [11], while a previous study conducted in 1990 on Ellesmere island provide an annual retreat of 9-14 m/y [19]. As discussed by Jones *et al.* 2019, the average retreat rates in the low Arctic are usually higher, as are RTS size. The most extensive RTS observed in this report covers 24 000 m<sup>2</sup> (RTS 20), and is very far from the so-called mega slumps covering areas between 5 and 40 ha observed in the low Arctic [18]. However, the RTS observed additionally in this report proved to be larger than those determined by Jones *et al.* 2019, which reached a maximum extension of about 17 000 m<sup>2</sup> (RTS 7).

### 6.2 Properties extraction

Permafrost roughly affects 24% of the earth's surface of the northern hemisphere, extending mainly between Alaska, Northern Canada and Russia [20]. However, the complexity of permafrost response precludes predictions other than on a local scale by taking individual slumps into account. An inventory of the slumps including their properties is therefore the only method to adequately estimate their impact on a global scale. Remote sensing represent a unique opportunity, being able to ensure the coverage of such an extensive area. Using digital elevation models, different features of the slumps can be outlined.

The induced volumetric change is a valid indicator to estimate the development and growth of thaw slumps. Considering both the headwall extension as well as the lowering of the slump floor, allow to estimate the amount of mobilized material. However, its use requires a careful correction of any height shifts and misalignment that may strongly influence the results, in particular in the case of RTS smaller than 10 000 m<sup>3</sup>. The retreat rates are another very interesting parameter to characterize the RTS activity, with perhaps the only weak point in not considering the variation of the slump floor. The headwall height instead provides little information about the development of the slumps, although it is useful to characterize its size. Retreats rates and headwall heights were not influenced by the vertical shift of the digital elevation models, and proved to be comparable to previous studies.

Since 1990, approximately 450 natural exposures of massive ice have been mapped only in the Eureka Sound area [10]. Due to the high occurrence and a predicted increase of permafrost thaw in the coming decades manual procedures do not allow to conduct studies on a regional scale. In order to achieve large scale inventories covering the whole pan-arctic region and therefore reaching better estimates of permafrost carbon feedback, the implementation of automatic methods is essential. An automatic RTSs detection method based on volumetric change has been presented by [8], showing promising opportunities for large scale mapping and to estimate the amount of material mobilized by the RTSs. Other approaches have used deep learning or vegetation variation as an indicator to detect slumps using optical data [21] [22]. The major challenge consists of an adequate classification of the detections, which requires large training data to achieve a sufficient accuracy. Nevertheless, accuracy greater than 80% has already been achieved in two of the three cases mentioned above [8] [22].

### 6.3 Data accuracy

Both ArcticDEM and TanDEM-X satellite systems have proven to be valid for monitoring retrogressive thaw slumps in the Canadian Arctic. A height accuracy of around two meters, as in the case of TanDEM-X, already allows to obtain a rather accurate estimate of the thaw slumps topography, considering that common headwall heights are generally between 5 and 10 meters. However, both have their limitations. Data from TanDEM-X observations are disadvantaged by lower resolution, which especially in the case of small RTS can be a determining factor in the accuracy of the measurements. Moreover, a higher variation of residues and a larger presence of random errors was observed. Arctic DEM data, on the other hand, require a snow-free landscape and a cloud-free sky, which significantly reduces the number of observations suitable. Furthermore, being also an active system, it depends on solar irradiation. Another limiting factor consist in a very fragmented spatial coverage, as shown in section 4, which makes it more complex to perform large-scale analysis. A variable accuracy between digital elevation models generated by ArcticDEM has also been observed, requiring a manual selection among the different observations, in order to obtain a better match with the previous years. This step represent an additional problem for the implementation of an automatic method for thaw slumps detection using ArcticDEM data. A higher accuracy in the alignment could have been increased by co-registering the data acquired to a reference DEM and adjusting the random height error of TanDEM-X by masking the pixel with a low coherence. Nevertheless, a satisfactory result in estimating the extent of permafrost thaw has already been possible without having to excessively correct the data. A major limitation is in the data availability, as RTSs may appear to behave differently depending on the timespan considered. Seasonal dynamics could only be accurately determined with regular observations at the beginning or end of the thaw season. In case of ArcticDEM, Data are currently available at irregular intervals, and often do not coincide with the frequency of RTS activity. In addition, the study throughout their entire life cycle is essential to properly understand their mechanisms.

Regular repeat observations could be ensured in the future by SESAME (SEntinel-1 SAR companion Multistatic Explorer) satellite mission proposed for the ESA Earth Explorer Program. Applying a similar concept as TanDEM-X, the mission aims to launch two receive-only C-band radar satellites to build a singlepass SAR interferometer using the active signal of Sentinel-1 satellite [23]. The main objective of the mission is to provide regular repeated generation of digital elevation models, which could substantially increase the potential of remote sensing applications in the fields of cryosphere, solid earth and biosphere.

## 7 Conclusion

Remote sensing has proven to be a very valuable tool to monitor retrogressive thaw slumps by comparing digital elevation models over time. Several slumps properties like the headwall height, retreat rates as well as the volumetric change can be detected, providing useful indicators to estimate the environmental impacts of permafrost degradation. In order to obtain precise measurements even with small thaw slumps, a careful co-registration of the individual DEMs is necessary. However, the major limitation has been identified as a lack of regular and repeated observations with a wide spatial coverage. Albeit ArcticDEM data displayed a higher accuracy and resolution compared to TanDEM-X data, their application for large scale studies was found to be rather limited by other factors, such as a limited area coverage of the single observations and a high sensitivity to weather conditions and snow coverage. Finally, the development of automatic methods for the detection and extraction of RTS properties is necessary in order to conduct research on a regional scale.

## References

- [1] T. Osterkamp, “Permafrost,” in *Encyclopedia of atmospheric sciences*, pp. 208–216, Amsterdam: Elsevier, Acad. Press, 2. ed ed., 2015.
- [2] S. V. Kokelj and M. T. Jorgenson, “Advances in Thermokarst Research: Recent Advances in Research Investigating Thermokarst Processes,” *Permafrost and Periglacial Processes*, vol. 24, pp. 108–119, Apr. 2013.
- [3] S. Zwieback, S. V. Kokelj, F. Günther, J. Boike, G. Grosse, and I. Hajnsek, “Sub-seasonal thaw slump mass wasting is not consistently energy limited at the landscape scale,” *The Cryosphere*, vol. 12, pp. 549–564, Feb. 2018.
- [4] L. Armstrong, D. Lacelle, R. H. Fraser, S. Kokelj, and A. Knudby, “Thaw slump activity measured using stationary cameras in time-lapse and Structure-from-Motion photogrammetry,” *Arctic Science*, vol. 4, pp. 827–845, Dec. 2018.
- [5] E. A. G. Schuur, A. D. McGuire, C. Schädel, G. Grosse, J. W. Harden, D. J. Hayes, G. Hugelius, C. D. Koven, P. Kuhrý, D. M. Lawrence, S. M. Natali, D. Olefeldt, V. E. Romanovsky, K. Schaefer, M. R. Turetsky, C. C. Treat, and J. E. Vonk, “Climate change and the permafrost carbon feedback,” *Nature*, vol. 520, pp. 171–179, Apr. 2015.
- [6] E. A. G. Schuur, J. G. Vogel, K. G. Crummer, H. Lee, J. O. Sickman, and T. E. Osterkamp, “The effect of permafrost thaw on old carbon release and net carbon exchange from tundra,” *Nature*, vol. 459, pp. 556–559, May 2009.
- [7] K. A. St. Pierre, S. Zolkos, S. Shakil, S. E. Tank, V. L. St. Louis, and S. V. Kokelj, “Unprecedented Increases in Total and Methyl Mercury Concentrations Downstream of Retrogressive Thaw Slumps in the Western Canadian Arctic,” *Environmental Science & Technology*, vol. 52, pp. 14099–14109, Dec. 2018.
- [8] P. Bernhard, S. Zwieback, S. Leinss, and I. Hajnsek, “An automated method for mapping retrogressive thaw slumps using single-pass TanDEM-X observations,” 2020.
- [9] E. a. C. C. Canada, “Station Results - Historical Data - Climate - Environment and Climate Change Canada.” [https://climate.weather.gc.ca/historical\\_data/search\\_historic\\_data\\_stations\\_e.html?searchType=stnName&timeframe=1&txtStationName=eureka&searchMethod=contains&optLimit=yearRange&StartYear=1840&EndYear=2020&Year=2020&Month=4&Day=20&selRowPerPage=25](https://climate.weather.gc.ca/historical_data/search_historic_data_stations_e.html?searchType=stnName&timeframe=1&txtStationName=eureka&searchMethod=contains&optLimit=yearRange&StartYear=1840&EndYear=2020&Year=2020&Month=4&Day=20&selRowPerPage=25). Accessed: May 2020.
- [10] W. Pollard, M. Ward, and M. Becker, “The Eureka Sound lowlands: an ice-rich permafrost landscape in transition,” 2015.
- [11] M. K. Ward Jones, W. H. Pollard, and B. M. Jones, “Rapid initialization of retrogressive thaw slumps in the Canadian high Arctic and their response to climate and terrain factors,” *Environmental Research Letters*, vol. 14, p. 055006, May 2019.
- [12] P. Rizzoli, M. Martone, C. Gonzalez, C. Wecklich, D. Borla Tridon, B. Bräutigam, M. Bachmann, D. Schulze, T. Fritz, M. Huber, B. Wessel, G. Krieger, M. Zink, and A. Moreira, “Generation and performance assessment of the global TanDEM-X digital elevation model,” *ISPRS Journal of Photogrammetry and Remote Sensing*, vol. 132, pp. 119–139, Oct. 2017.

- [13] G. Krieger, M. Zink, M. Bachmann, B. Bräutigam, D. Schulze, M. Martone, P. Rizzoli, U. Steinbrecher, J. Walter Antony, F. De Zan, I. Hajnsek, K. Papathanassiou, F. Kugler, M. Rodriguez Cassola, M. Younis, S. Baumgartner, P. López-Dekker, P. Prats, and A. Moreira, “TanDEM-X: A radar interferometer with two formation-flying satellites,” *Acta Astronautica*, vol. 89, pp. 83–98, Aug. 2013.
- [14] C. Porter, P. Morin, I. Howat, M.-J. Noh, B. Bates, K. Peterman, S. Keesey, M. Schlenk, J. Gardiner, K. Tomko, M. Willis, C. Kelleher, M. Cloutier, E. Husby, S. Foga, H. Nakamura, M. Platson, M. Wethington, C. Williamson, G. Bauer, J. Enos, G. Arnold, W. Kramer, P. Becker, A. Doshi, C. D’Souza, P. Cummens, F. Laurier, and M. Bojesen, “ArcticDEM,” 2018. type: dataset.
- [15] P. G. center, “Introduction to stereoscopic imagery.” <https://www.pgc.umn.edu/guides/stereo-derived-elevation-models/introduction-to-stereoscopic-imagery/>. Accessed: May 2020.
- [16] “SETSM.” <https://mjremotesensing.wordpress.com/setsm/>, Feb. 2017. Accessed: May 2020.
- [17] M. K. E. Himmelstoss, R. Henderson and A. Farris, “Digital shoreline analysis system: Version 5.0 user guide,” *U.S. Geological Survey*, 2018.
- [18] S. Kokelj, J. Tunnicliffe, D. Lacelle, T. Lantz, K. Chin, and R. Fraser, “Increased precipitation drives mega slump development and destabilization of ice-rich permafrost terrain, northwestern Canada,” *Global and Planetary Change*, vol. 129, pp. 56–68, June 2015.
- [19] Lewkowicz, “Morphology, frequency and magnitude of active-layer detachment slides, fosheim peninsula, ellesmere island, nwt,” *Proc. 5th Canadian Permafrost Conf.*, vol. 54, 1990.
- [20] I. Nitze, G. Grosse, B. M. Jones, V. E. Romanovsky, and J. Boike, “Remote sensing quantifies widespread abundance of permafrost region disturbances across the Arctic and Subarctic,” *Nature Communications*, vol. 9, p. 5423, Dec. 2018.
- [21] L. Huang, L. Liu, L. Jiang, and T. Zhang, “Automatic Mapping of Thermokarst Landforms from Remote Sensing Images Using Deep Learning: A Case Study in the Northeastern Tibetan Plateau,” *Remote Sensing*, vol. 10, p. 2067, Dec. 2018.
- [22] M. J. Lara, M. L. Chipman, and F. S. Hu, “Automated detection of thermoerosion in permafrost ecosystems using temporally dense Landsat image stacks,” *Remote Sensing of Environment*, vol. 221, pp. 462–473, Feb. 2019.
- [23] H. Rott, P. Lopez-Dekker, S. Solberg, L. Ulander, T. Nagler, G. Krieger, P. Prats, M. Rodriguez, M. Zonno, and A. Moreira, “SESAME: A single-pass interferometric SEntinel-1 companion SAR mission for monitoring GEO-and biosphere dynamics,” in *2017 IEEE International Geoscience and Remote Sensing Symposium (IGARSS)*, (Fort Worth, TX), pp. 107–110, IEEE, July 2017.

# Appendices

## A RTS locations

### Sector A



**Table A1:** Exact Coordinates of the RTS locations in sector A.

RTS	Latitude	Longitude
1	80° 00'02.93"	85° 52'26.64"
2	79° 59'51.43"	85° 53'42.94"
3	79° 59'50.52"	85° 52'57.88"
4	79° 59'45.86"	85° 53'02.21"
5	79° 59'41.84"	85° 53'15.71"
6	79° 59'31.82"	85° 52'47.73"

**Figure A1:** Sector A

### Sector B



**Table A2:** Exact Coordinates of the RTS locations in sector B.

RTS	Latitude	Longitude
7	79° 59'09.30"	85° 48'02.55"
8	79° 59'15.26"	85° 47'09.94"
9	79° 59'11.51"	85° 46'14.74"
10	79° 58'58.22"	85° 47'17.06"
11	79° 58'59.34"	85° 44'21.48"
12	79° 59'08.87"	85° 42'05.59"
20	79° 59'59.58"	85° 40'49.49"

**Figure A2:** Sector B

### Sector C

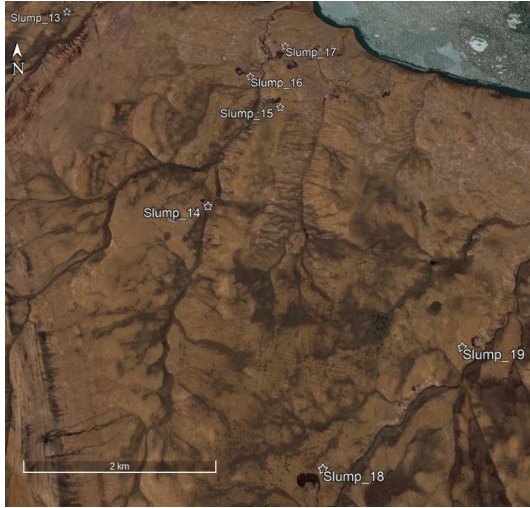


**Table A3:** Exact Coordinates of the RTS locations in sector C.

RTS	Latitude	Longitude
13	79° 57'17.66"	85° 59'11.89"
14	79° 55'39.60"	86° 02'55.29"
15	79° 56' 29.10"	85° 59'56.23"
16	79° 56'43.99"	86° 01'25.86"
17	79° 56'54.77"	85° 59'41.45"
18	79° 53'51.30"	85° 59'11.89"
19	79° 54'39.32"	85° 53'18.20"

**Figure A3:** Sector C

## B Data Specifications

**Table A4:** Specifications of the exact observation used. All mapping methods used are obtained from satellite imagery, generated from the panchromatic bands of the WorldView-1 (WV01), WorldView-2 (WV02), WorldView-3 (WV03) and in small percentage from the GeoEye-1 (GE01) satellite sensor.

Date	stripDemId	Sensor	RTS Mapped
10.08.2009		GE01	13, 14, 15-17, 18,19
12.08.2009		GE01	1-6, 20
02.07.2010		W2W2	13, 14, 1-6,18, 20
11.08.2011		WV02	1-6,13, 14, 15-17,18,19
14.08.2012		WV02	1-6, 14, 15-17,18, 19 20
27.08.2012		WV02	13
01.08.2013		WV01	13, 14, 15-17,18, 19 20
12.09.2013		WV02	1-6
03.07.2014		WV02	20
01.08.2014		WV01	1-6, 13, 14, 15-17,18, 19
08.07.2016		WV02	20
01.01.2017		TanDEM-X	1-20

## C Data availability

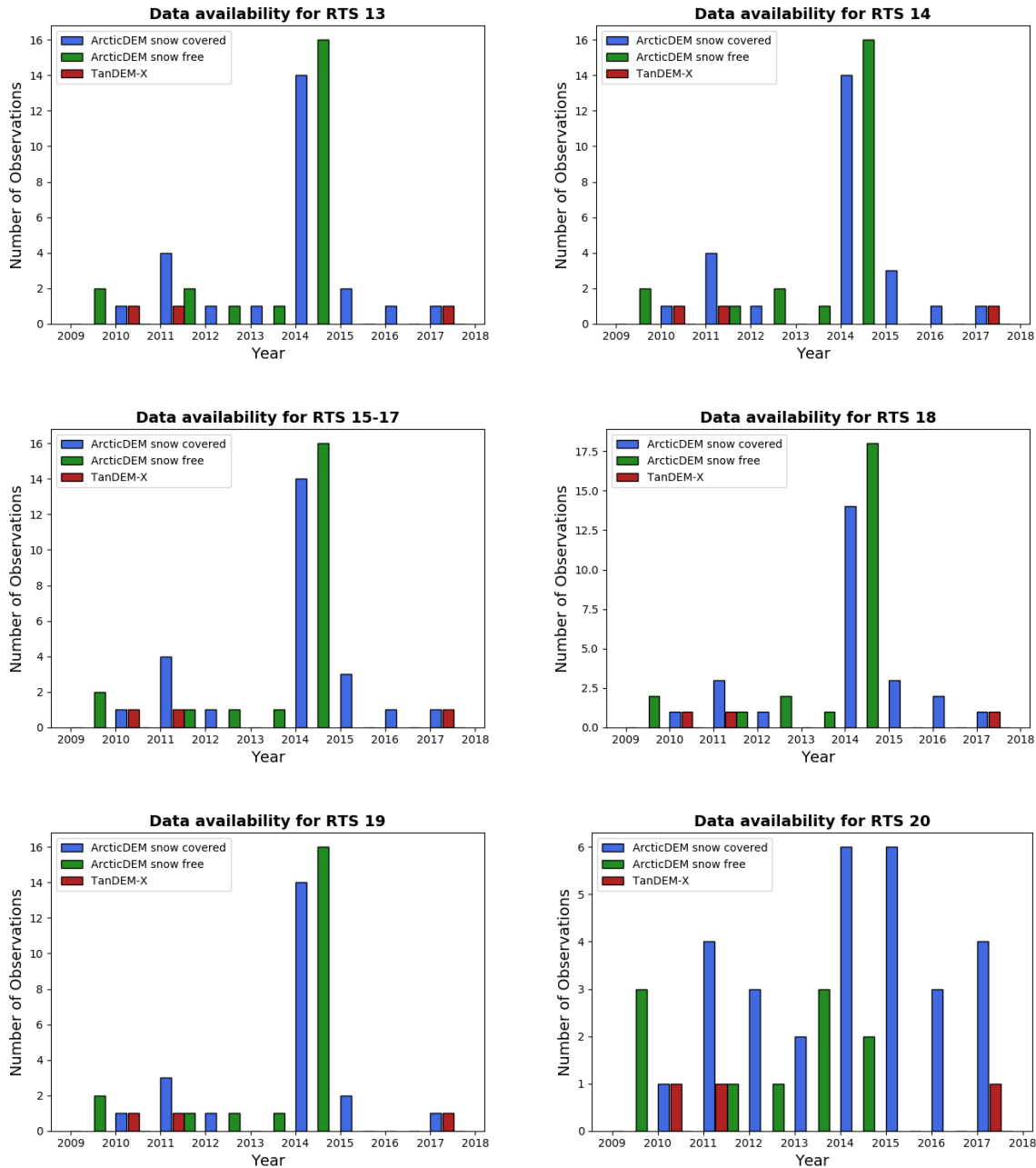


**Figure A4:** Data Availability of the researched area. The landscape was assumed snow free from the mid of july to september. Tandem-X observation where made in winter (2017 means winter 2016-2017).

## D Accuracy statistics

### Test area 1

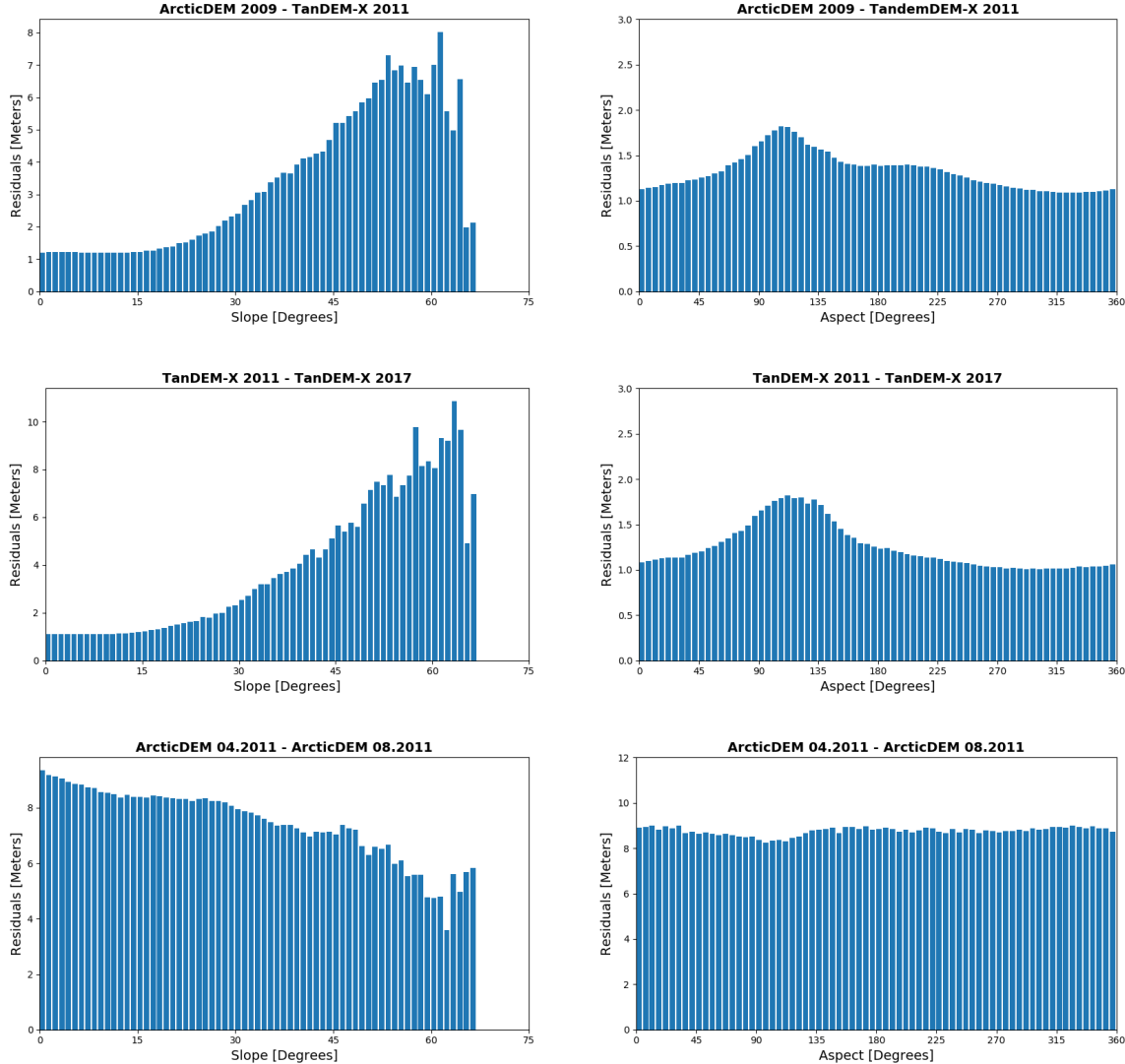


**Figure A5:** Remaining accuracy statistics computed on test area 1. In the case of the aspect, 0 degrees indicates the north direction. ArcticDEM acquired in summer and TanDEM-X data show similar trends, while optical measurements in spring are strongly affected from snow.

## Test area 2

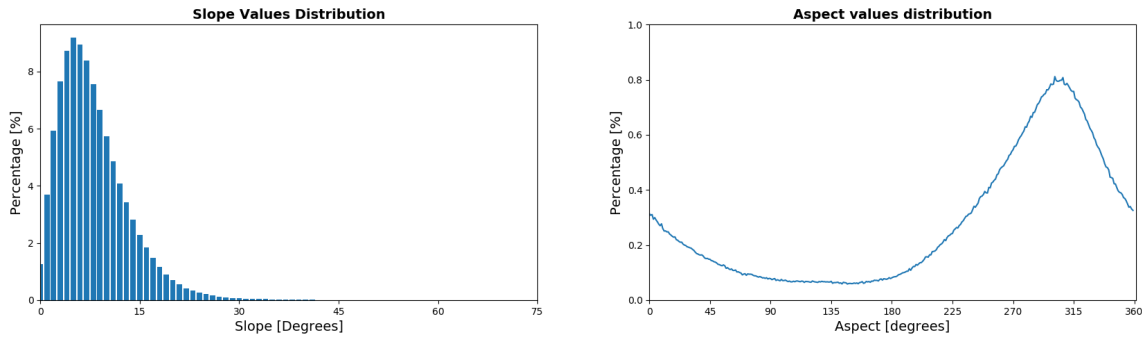


**Figure A6:** Values distribution determined for Area 2. In the case of the aspect, 0 degrees indicates north direction.

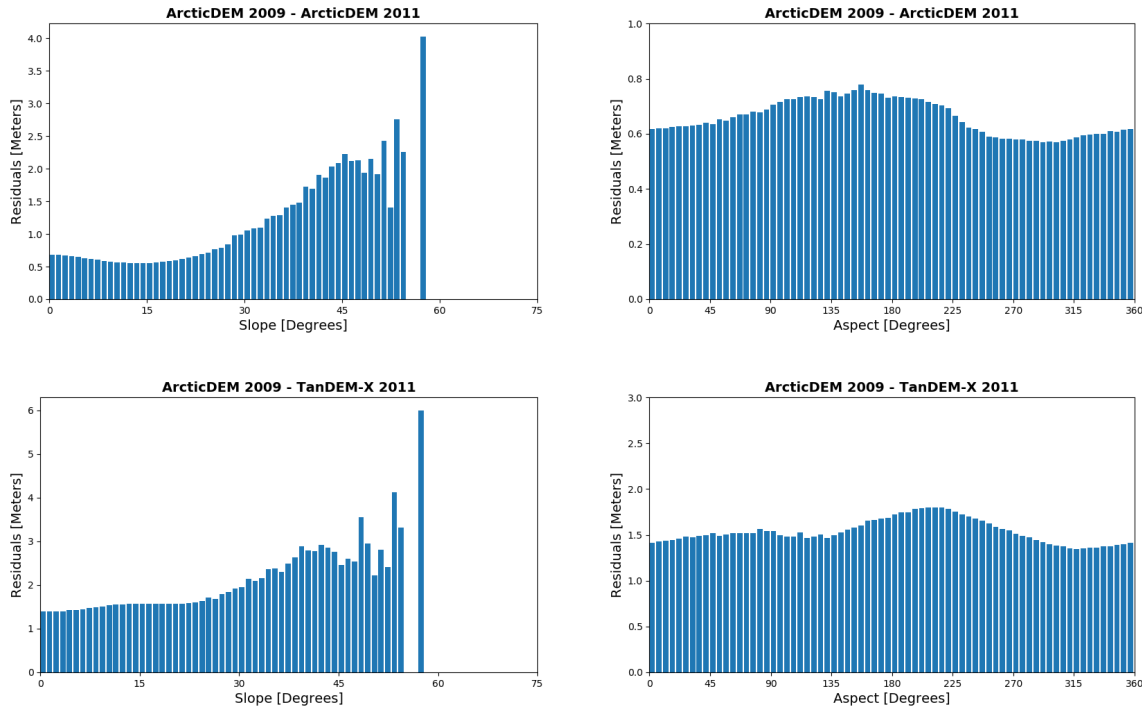


**Figure A7:** Accuracy statistics computed on Area 2. In the case of the aspect, 0 degrees indicates the north direction.

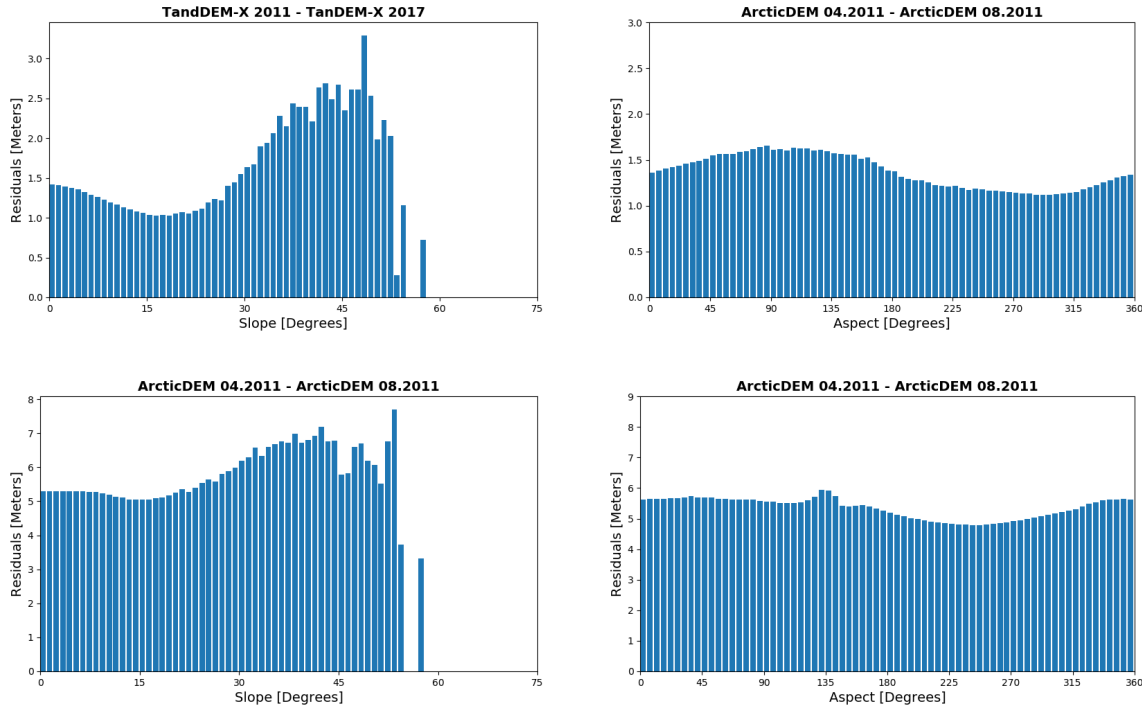


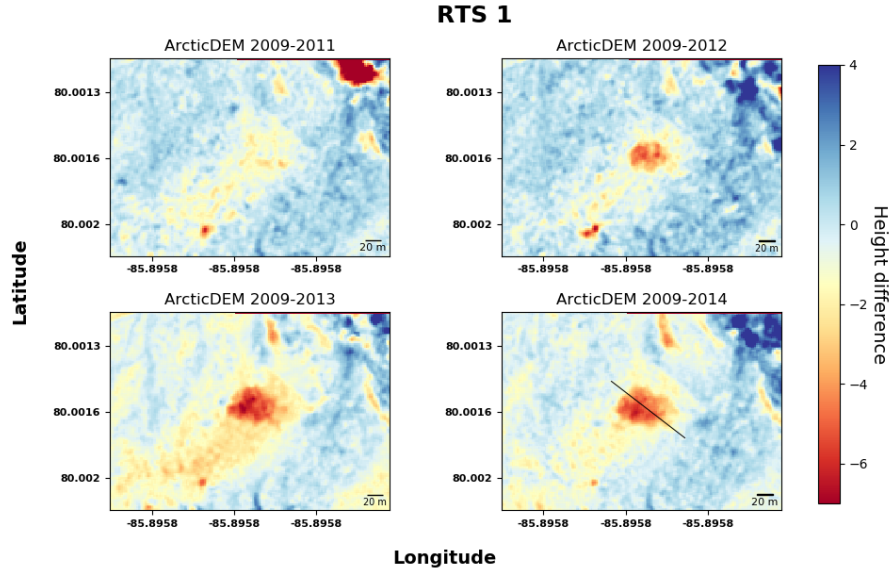
**Figure A8:** Remaining accuracy statistics computed on Area 2. Accuracy statistics computed on test area 1. In the case of the aspect, 0 degrees indicates the north direction.

## E Additional Locations

The following pages contain all the slumps analysed, with the exception of the RTS 18 which was entirely presented in the main text. In some cases the difference images between 2009-2010 were not included because they did not contain relevant information. Regarding those generated between 2009 and 2017, they were excluded in case the images were affected by random errors that did not allow to generate clear images. In the case of RTS 14 it was not possible to determine the headwall height in the period 2009-2017 due to too many differences between the two DEMs.

It is interesting to note that some slumps show particular behaviour. The headwall of RTS 2 is ablated along several sections over the years, resulting in a retreat that does not follow a single direction. In this case the measurement of the headwall retreat was challenging, since the transects couldn't be generated along the whole headwall. The particular shape of RTS 17, which presents unthawed permafrost in its center, leads it to develop in two directions along the transect line. Due to the topography of the terrain, RTS 20 also presents an unusual development, with a rapid retreat in the years following 2014.

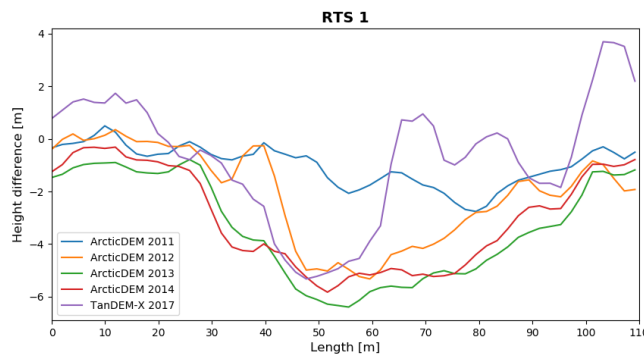
## RTS 1



**Figure 9:** Difference image

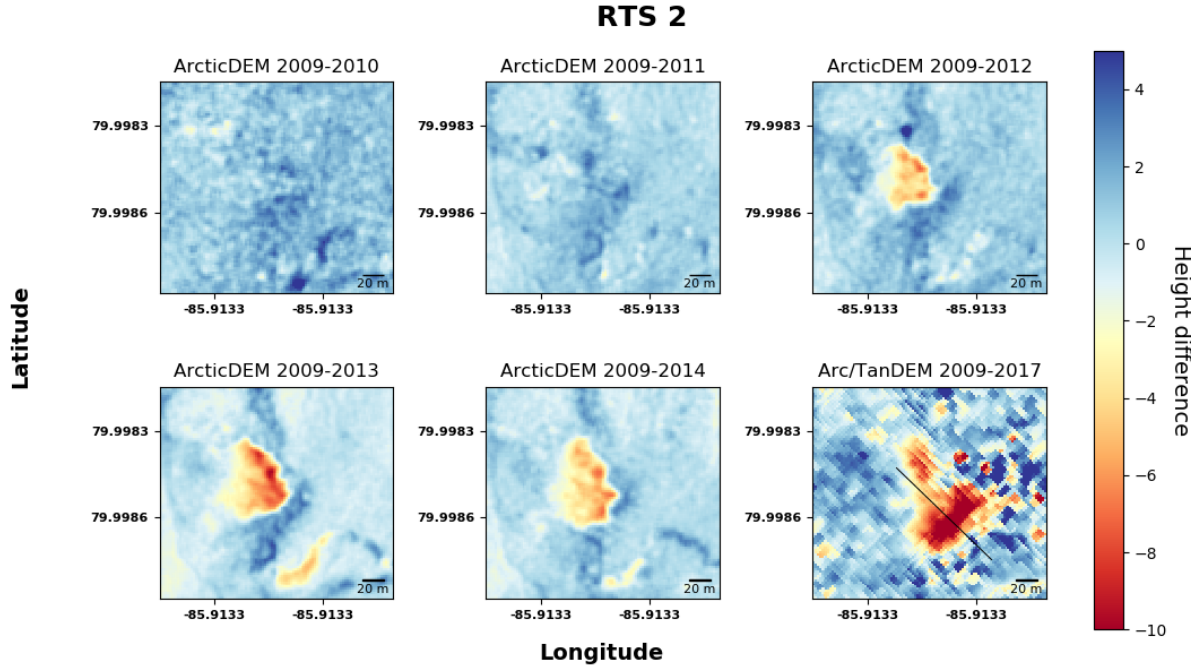
**Table 5:** Properties of RTS 1

Time period	Area [m <sup>2</sup> ]	Vol. change [10 <sup>3</sup> m <sup>3</sup> ]	Headwall Height [m]	Headwall Retreat [m]	TDD [°C]
02.07.2010-11.08.2011	980	3	1.9	Init.	900.5
11.08.2011-14.08.2012	1200	4.6	5	13.3	616.8
14.08.2012-12.09.2013	2190	10.5	5.6	10.5	313.1
12.09.2013-01.08.2014	2176	9.5	4.6	2.8	247.1
01.08.2014-01.01.2017	2780	6.4	6.8	0.6	1292.8



**Figure 10:** Profile along the transect line

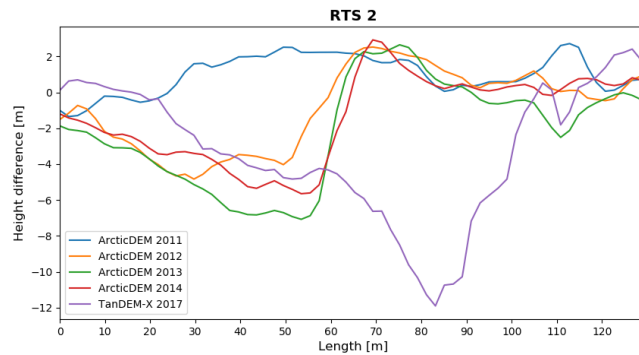
## RTS 2



**Figure 11:** Difference image

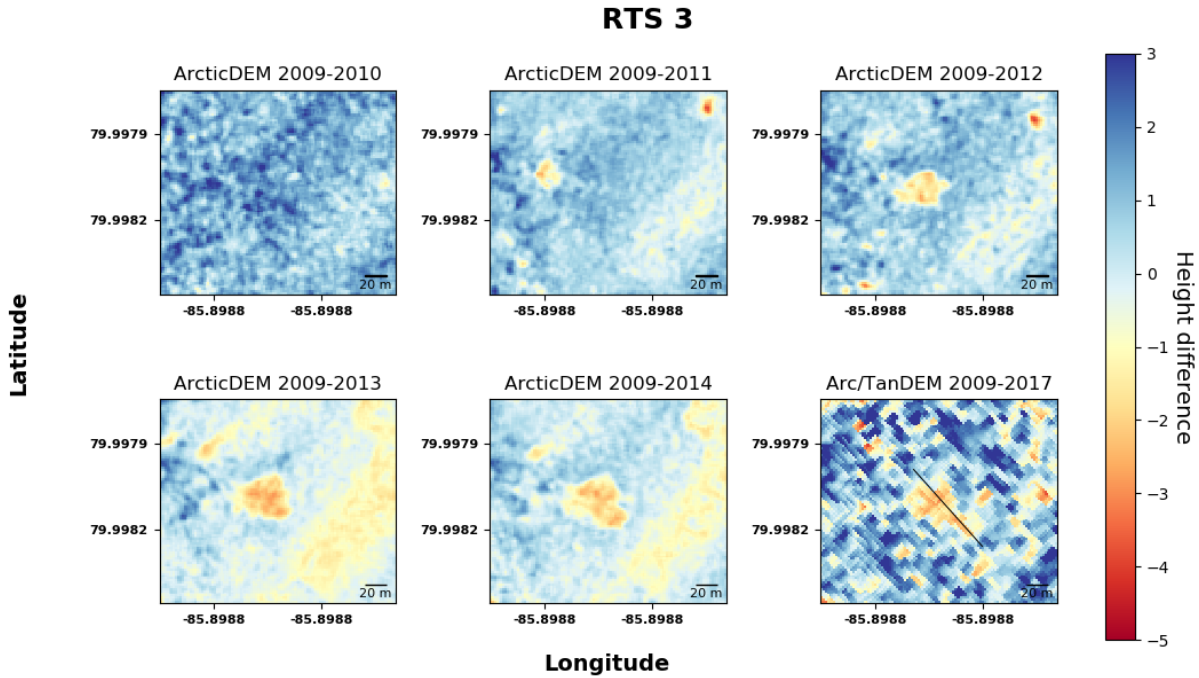
**Table 6:** Properties of RTS 2

Time period	Area [m <sup>2</sup> ]	Vol. change [10 <sup>3</sup> m <sup>3</sup> ]	Headwall Height [m]	Headwall Retreat [m]	TDD [°C]
02.07.2010-11.08.2011	3388	0.2	1.7	Init.	900.5
11.08.2011-14.08.2012	2916	7.2	6.5	15.7	616.8
14.08.2012-12.09.2013	2920	13.5	9.7	6.5	313.1
12.09.2013-01.08.2014	3356	12.0	8.5	4.8	247.1
01.08.2014-01.01.2017	8644	36.2	10.7	28.3	1292.8



**Figure 12:** Profile along the transect line

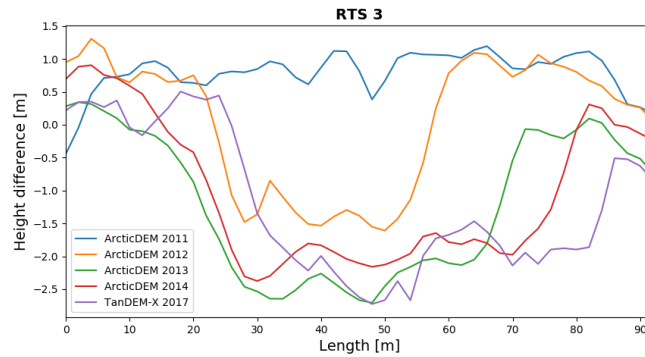
## RTS 3



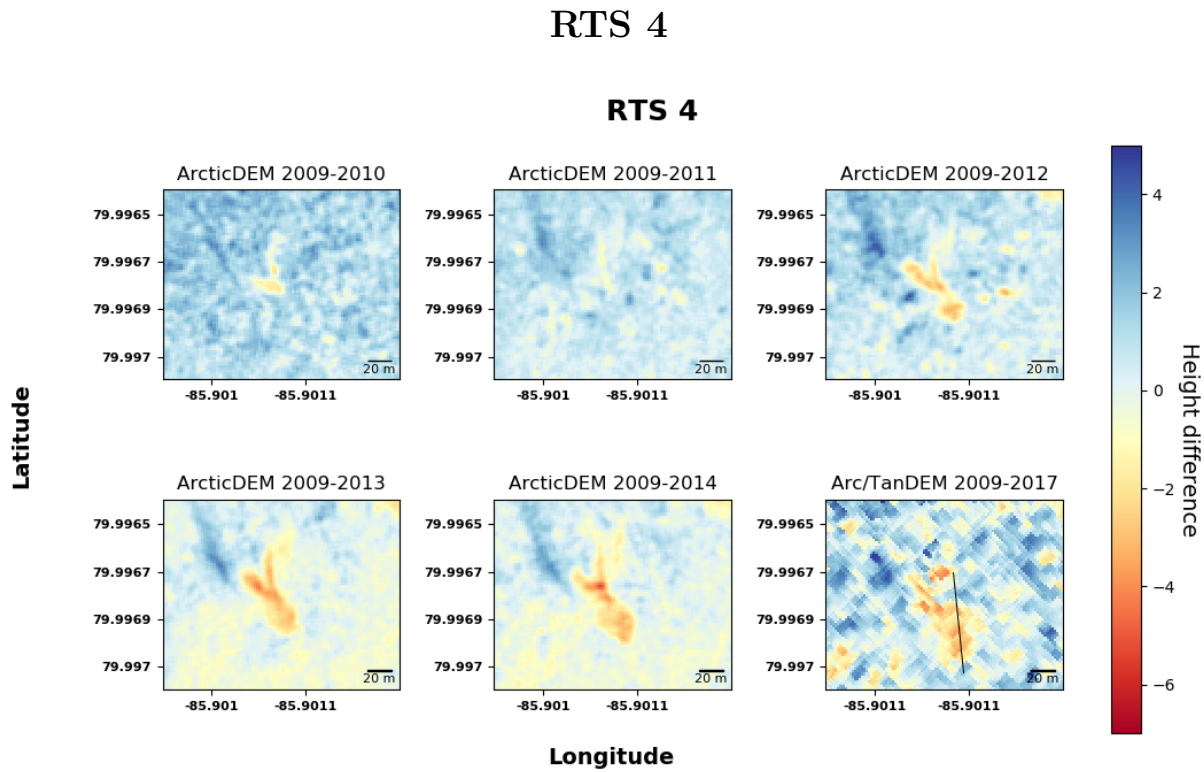
**Figure 13:** Difference image

**Table 7:** Properties of RTS 3

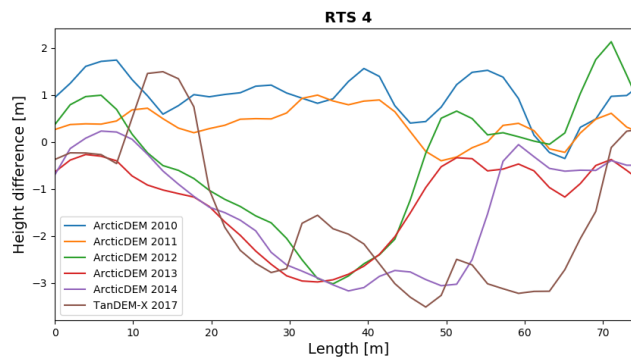
Time period	Area [m <sup>2</sup> ]	Vol. change [10 <sup>3</sup> m <sup>3</sup> ]	Headwall Height [m]	Headwall Retreat [m]	TDD [°C]
02.07.2010-11.08.2011	408	0.5	-	Init.	900.5
11.08.2011-14.08.2012	1220	1.5	2.7	24.2	616.8
14.08.2012-12.09.2013	1648	2.9	2.3	3.8	313.1
12.09.2013-01.08.2014	1616	2.6	2.3	7.3	247.1
01.08.2014-01.01.2017	2480	3.0	1.8	9.4	1292.8



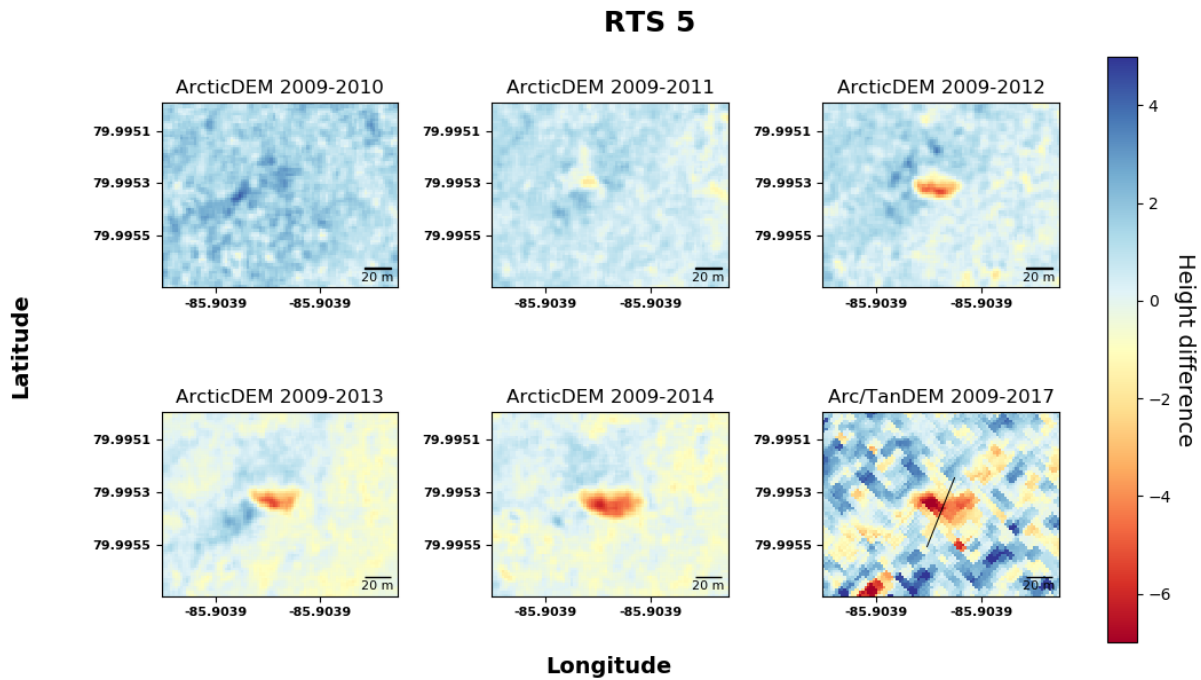
**Figure 14:** Profile along the transect line

**Figure 15:** Difference image**Table 8:** Properties of RTS 4

Time period	Area [m <sup>2</sup> ]	Vol. change [10 <sup>3</sup> m <sup>3</sup> ]	Headwall Height [m]	Headwall Retreat [m]	TDD [°C]
02.07.2010-11.08.2011	292	0.2	-	Init.	900.5
11.08.2011-14.08.2012	824	1.7	3.6	11.3	616.8
14.08.2012-12.09.2013	1320	3.2	2.7	3.2	313.1
12.09.2013-01.08.2014	1372	3.1	3	5.2	247.1
01.08.2014-01.01.2017	2964	4.9	3.5	11.7	1292.8

**Figure 16:** Profile along the transect line

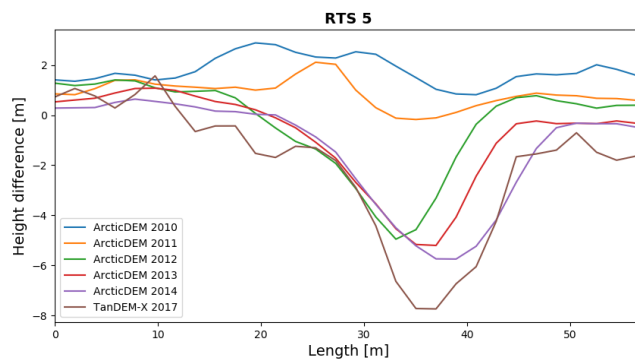
## RTS 5



**Figure 17:** Difference image

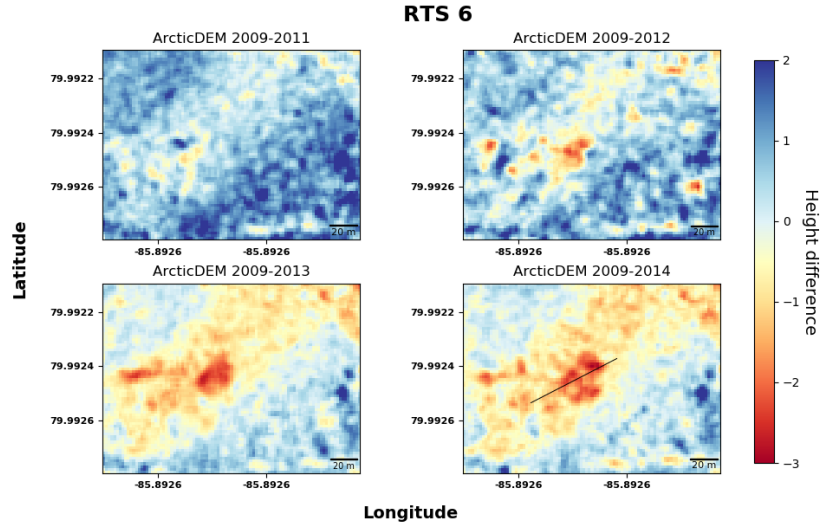
**Table 9:** Properties of RTS 5

Time period	Area [m <sup>2</sup> ]	Vol. change [10 <sup>3</sup> m <sup>3</sup> ]	Headwall Height [m]	Headwall Retreat [m]	TDD [°C]
02.07.2010-11.08.2011	228	0.1	1.5	Init.	900.5
11.08.2011-14.08.2012	736	1.4	5.7	8.2	616.8
14.08.2012-12.09.2013	680	1.7	5.0	2.4	313.1
12.09.2013-01.08.2014	820	2.9	5.5	6.1	247.1
01.08.2014-01.01.2017	1104	3.9	5.3	2.7	1292.8



**Figure 18:** Profile along the transect line

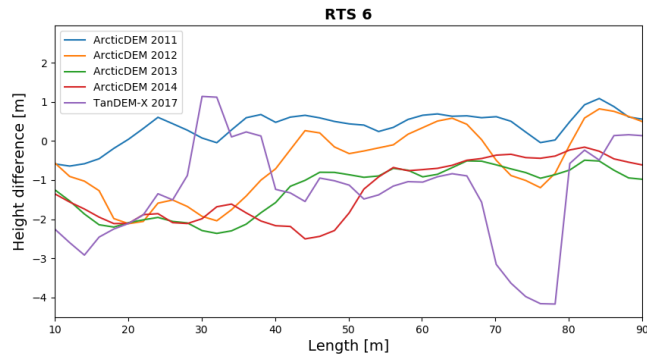
## RTS 6



**Figure 19:** Difference image

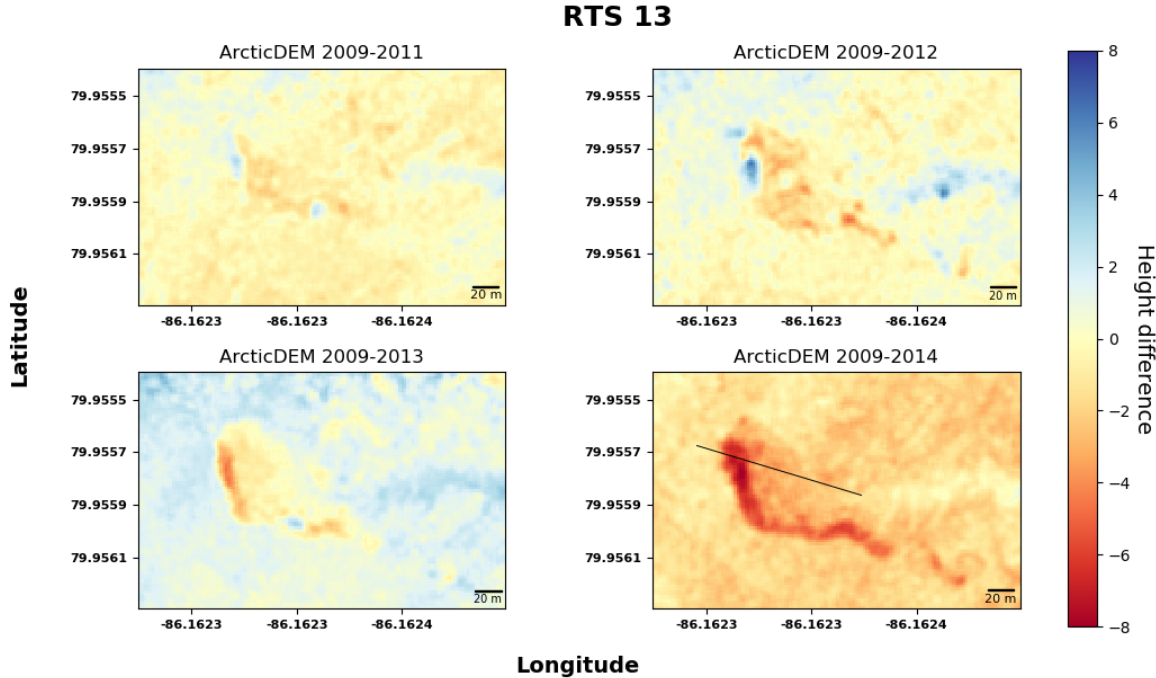
**Table 10:** Properties of RTS 6

Time period	Area [m <sup>2</sup> ]	Vol. change [10 <sup>3</sup> m <sup>3</sup> ]	Headwall Height [m]	Headwall Retreat [m]	TDD [°C]
02.07.2010-11.08.2011	64	0.1	-	Init.	900.5
11.08.2011-14.08.2012	816	0.8	2.2	19.4	616.8
14.08.2012-12.09.2013	908	1.6	1.8	3.7	313.1
12.09.2013-01.08.2014	996	1.9	2.1	7.0	247.1
01.08.2014-01.01.2017	1832	2.8	3.1	9.2	1292.8



**Figure 20:** Profile along the transect line

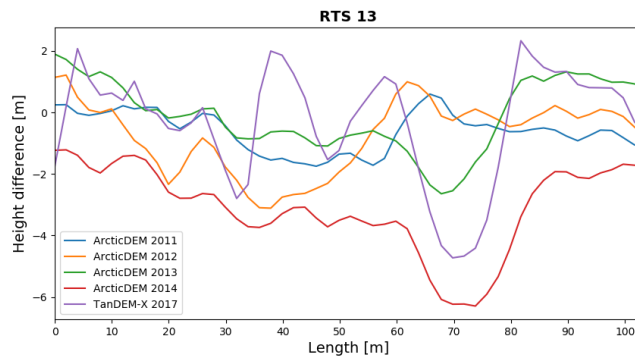
## RTS 13



**Figure 21:** Difference image

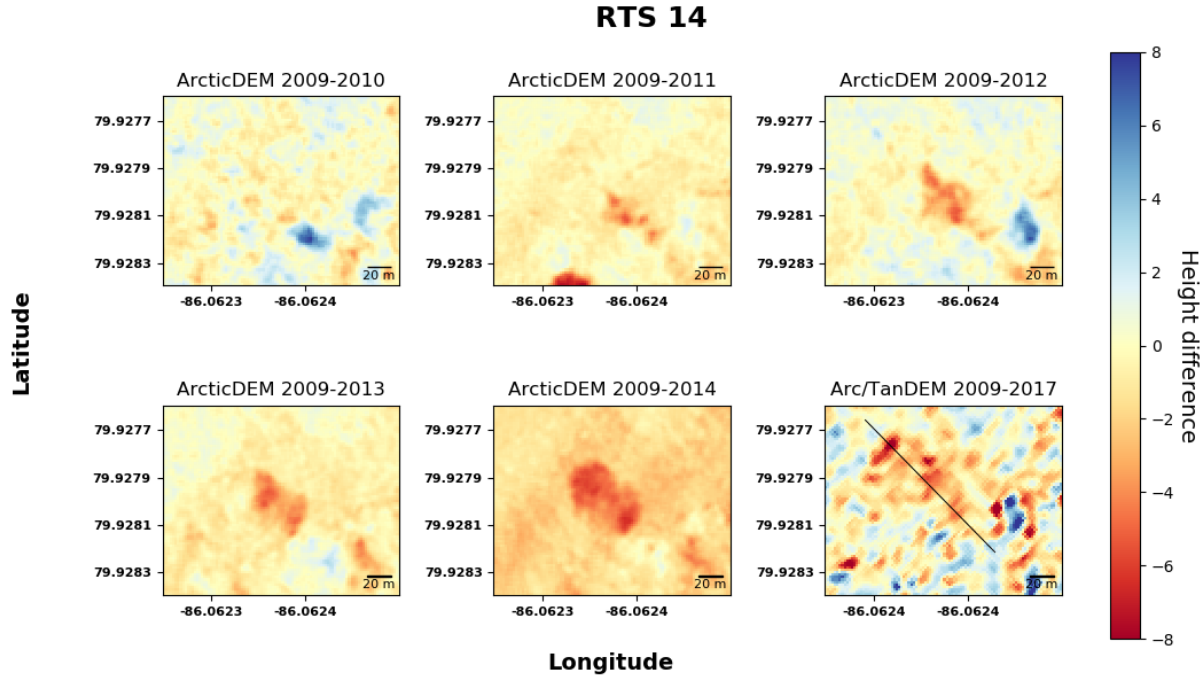
**Table 11:** Properties of RTS 13

Time period	Area [m <sup>2</sup> ]	Vol. change [10 <sup>3</sup> m <sup>3</sup> ]	Headwall Height [m]	Headwall Retreat [m]	TDD [°C]
02.07.2010-11.08.2011	1296	1.9	-	Init.	900.5
11.08.2011-14.08.2012	2276	4.6	3.5	8.5	681.6
14.08.2012-01.08.2013	2144	3.2	3.4	8.3	208.3
01.08.2013-01.08.2014	3560	16.5	4.2	10.1	279.21
01.08.2014-01.01.2017	2948	12.4	5.4	7.4	1292.8



**Figure 22:** Profile along the transect line

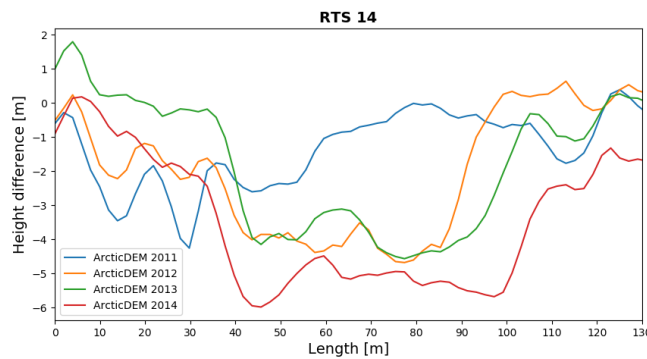
## RTS 14



**Figure 23:** Difference image

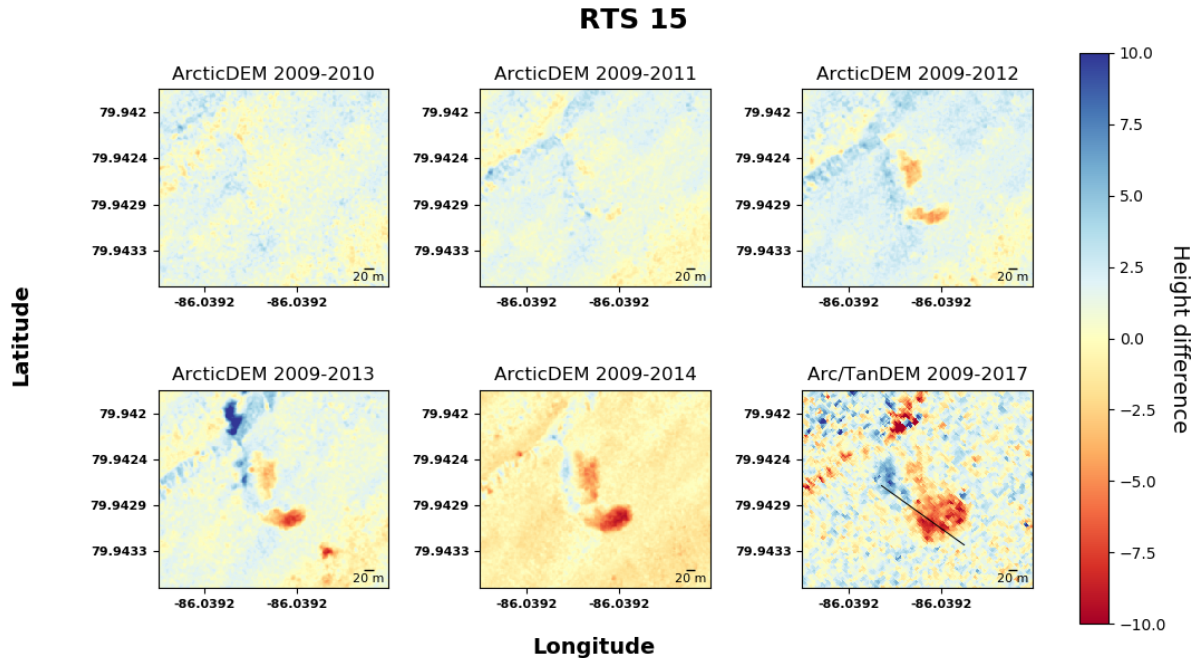
**Table 12:** Properties of RTS 14

Time period	Area [m <sup>2</sup> ]	Vol. change [10 <sup>3</sup> m <sup>3</sup> ]	Headwall Height [m]	Headwall Retreat [m]	TDD [°C]
02.07.2010-11.08.2011	884	2.6	-	Init.	900.5
11.08.2011-14.08.2012	2000	5.6	4.4	22.8	616.8
14.08.2012-01.08.2013	1684	5.7	4.5	9.2	272.6
01.08.2013-01.08.2014	2416	11.2	4.4	10.1	292.1
01.08.2014-01.01.2017	2932	10.3	N.A	30.6	1292.8



**Figure 24:** Profile along the transect line

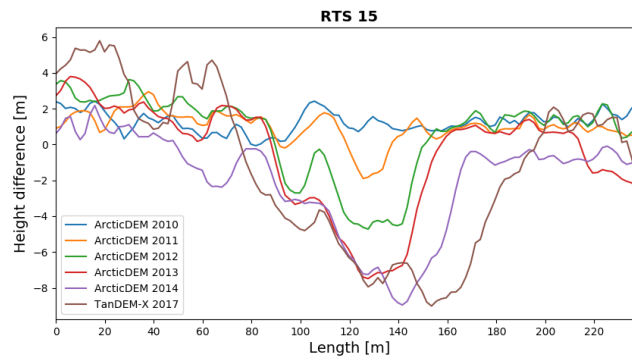
## RTS 15



**Figure 25:** Difference image

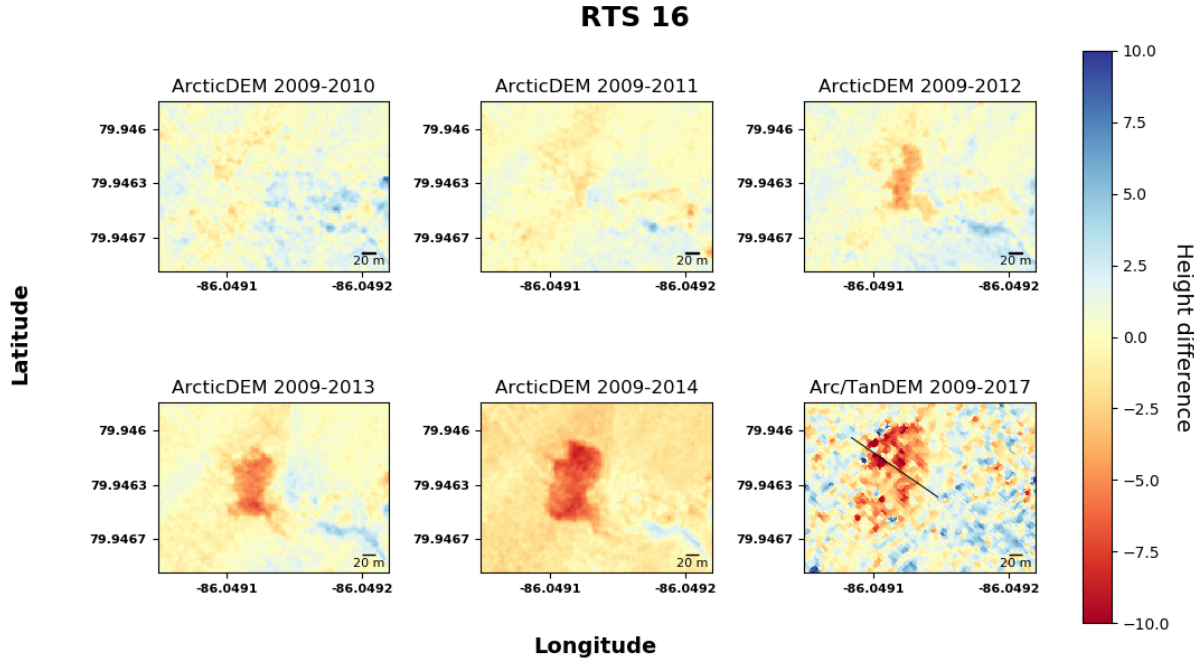
**Table 13:** Properties of RTS 15

Time period	Area [ $10^3 \text{m}^2$ ]	Vol. change [ $10^3 \text{m}^3$ ]	Headwall Height [m]	Headwall Retreat [m]	TDD [ $^{\circ}\text{C}$ ]
02.07.2010-11.08.2011	-	-	(3.4)	Init.	900.5
11.08.2011-14.08.2012	2.6	8.3	6.3	10.6	616.8
14.08.2012-01.08.2013	3.6	14.8	8.0	6.2	272.6
01.08.2013-01.08.2014	5.7	30.7	8.3	10.1	292.1
01.08.2014-01.01.2017	12.6	56.8	11	17.7	1292.8



**Figure 26:** Profile along the transect line

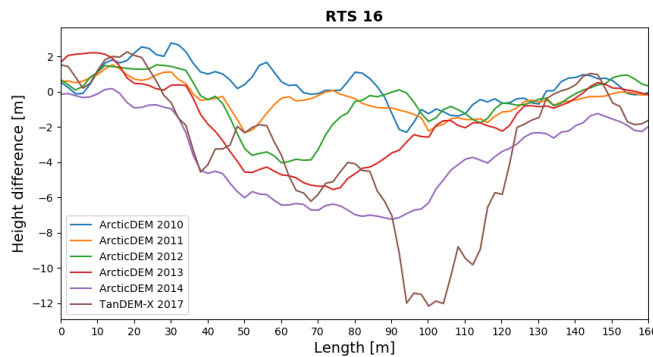
## RTS 16



**Figure 27:** Difference image

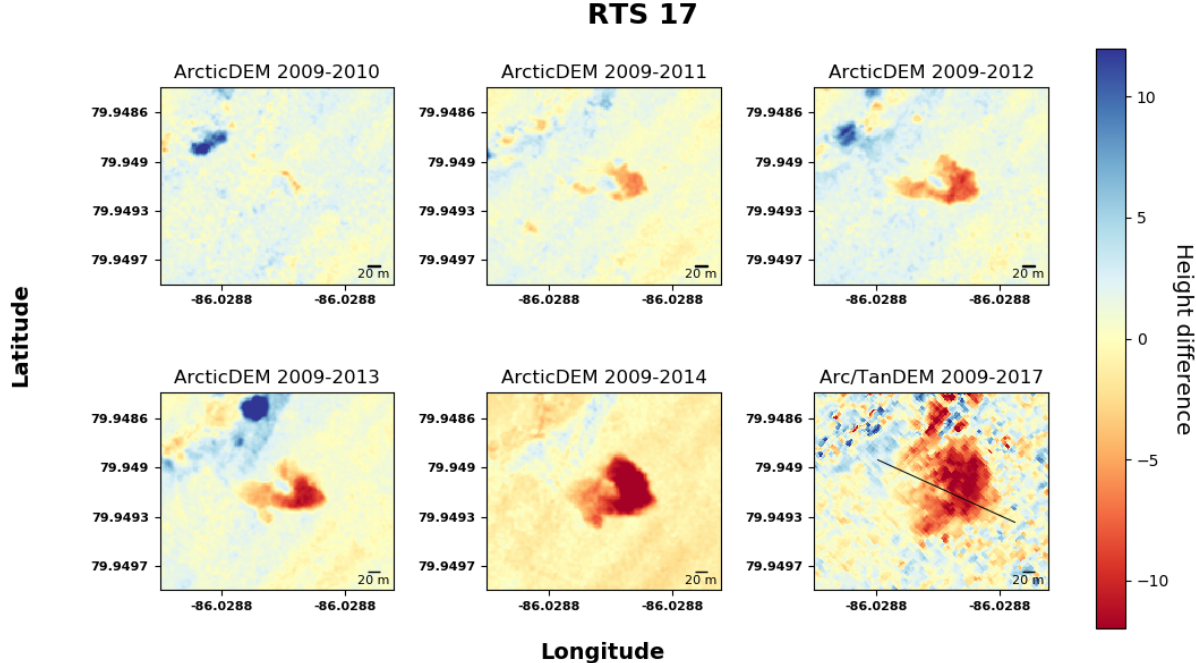
**Table 14:** Properties of RTS 16

Time period	Area [m <sup>2</sup> ]	Vol. change [10 <sup>3</sup> m <sup>3</sup> ]	Headwall Height [m]	Headwall Retreat [m]	TDD [°C]
02.07.2010-11.08.2011	676	1.1	1.9	Init.	900.5
11.08.2011-14.08.2012	4036	11.9	3.9	13.3	616.8
14.08.2012-01.08.2013	4968	22.3	3.9	12.6	272.6
01.08.2013-01.08.2014	7544	44.6	4.7	11.7	292.1
01.08.2014-01.01.2017	14576	51.9	12.4	17.8	1292.8



**Figure 28:** Profile along the transect line

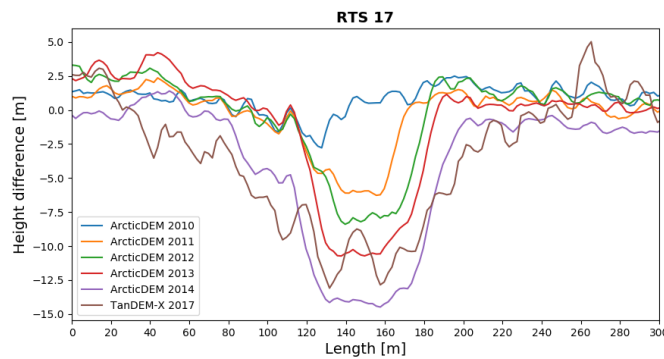
## RTS 17



**Figure 29:** Difference image

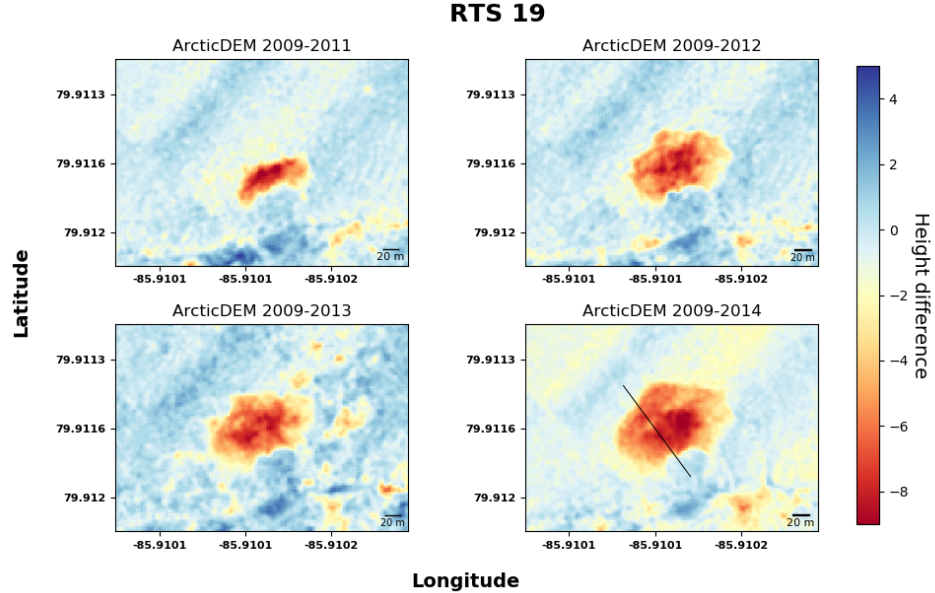
**Table 15:** Properties of RTS 17

Time period	Area [m <sup>2</sup> ]	Vol. change [10 <sup>3</sup> m <sup>3</sup> ]	Headwall Height [m]	Headwall Retreat [m]	TDD [°C]
02.07.2010-11.08.2011	2260	9.9	6.2	Init.	900.5
11.08.2011-14.08.2012	4968	27.1	9	7.1	616.8
14.08.2012-01.08.2013	5364	32.8	11.1	6.6	272.6
01.08.2013-01.08.2014	9376	86.0	12.5	8.3	292.1
01.08.2014-01.01.2017	18208	128.3	12.1	17.9	1292.8



**Figure 30:** Profile along the transect line

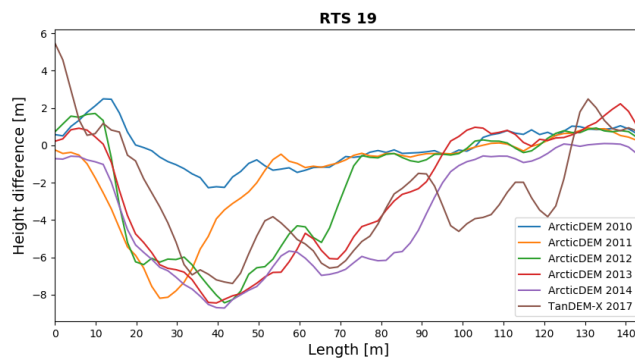
## RTS 19



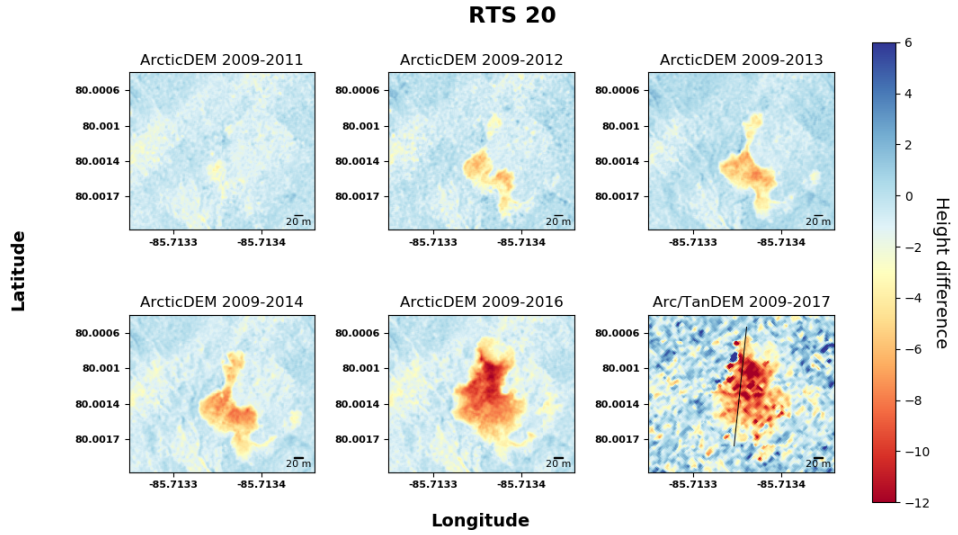
**Figure 31:** Difference image

**Table 16:** Properties of RTS 19

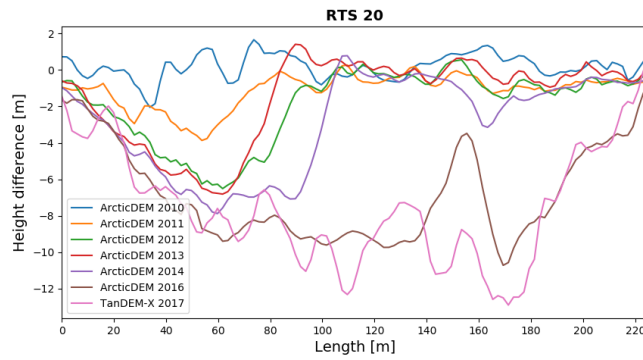
Time period	Area [10 <sup>3</sup> m <sup>2</sup> ]	Vol. change [10 <sup>3</sup> m <sup>3</sup> ]	Headwall Height [m]	Headwall Retreat [m]	TDD [°C]
02.07.2010-11.08.2011	2.7	14.5	7.2	Init.	900.5
11.08.2011-14.08.2012	5.8	31.5	7.5	33.4	616.8
14.08.2012-01.08.2013	7.1	35.4	7.4	4.4	272.6
01.08.2013-01.08.2014	8.1	47.1	6.8	11.0	292.1
01.08.2014-01.01.2017	12.7	42.7	6.5	29.0	1292.8



**Figure 32:** Profile along the transect line

**RTS 20****Figure 33:** Difference image**Table 17:** Properties of RTS 20

Time period	Area [ $10^3 \text{m}^2$ ]	Vol. change [ $10^3 \text{m}^3$ ]	Headwall Height [m]	Headwall Retreat [m]	TDD [ $^{\circ}\text{C}$ ]
02.07.2010-11.08.2011	1.6	3.7	3.2	Init.	900.5
11.08.2011-14.08.2012	5.7	26.0	5.5	17.1	616.8
14.08.2012-01.08.2013	8.7	42.1	7.8	21.7	272.6
01.08.2013-01.08.2014	10.4	59.1	7.8	11.7	118
01.08.2014-08.07.2016	20.9	145.4	9.7	63.9	1064.9
08.07.2016-01.01.2017	24.4	167.7	12.3	16.7	413.7

**Figure 34:** Profile along the transect line

**Declaration of originality**

The signed declaration of originality is a component of every semester paper, Bachelor's thesis, Master's thesis and any other degree paper undertaken during the course of studies, including the respective electronic versions.

Lecturers may also require a declaration of originality for other written papers compiled for their courses.

I hereby confirm that I am the sole author of the written work here enclosed and that I have compiled it in my own words. Parts excepted are corrections of form and content by the supervisor.

**Title of work** (in block letters):

Property extraction of retrogressive thaw slumps in the Canadian high Arctic using TanDEM-X & ArcticDEM data

**Authored by** (in block letters):

*For papers written by groups the names of all authors are required.*

Name(s):

Lagli

First name(s):

Giorgio

With my signature I confirm that

- I have committed none of the forms of plagiarism described in the 'Citation etiquette' information sheet.
- I have documented all methods, data and processes truthfully.
- I have not manipulated any data.
- I have mentioned all persons who were significant facilitators of the work.

I am aware that the work may be screened electronically for plagiarism.

Place, date

23.05.2020 Cana

Signature(s)

*For papers written by groups the names of all authors are required. Their signatures collectively guarantee the entire content of the written paper.*